Variability of Isotope Composition of Precipitation in the Southeastern Tibetan Plateau from the Synoptic to Seasonal Time Scale

Xiaoyi Shi, Camille Risi, Tao Pu, Jean-lionel Lacour, Yanlong Kong, Ke Wang, Yuanqing He, Dunsheng Xia

Shi Xiaoyi (Orcid ID: 0000-0003-1503-0088)

Risi Camille (Orcid ID: 0000-0002-8267-453X)

Pu Tao (Orcid ID: 0000-0002-1876-1487)

Lacour Jean-Lionel (Orcid ID: 0000-0003-3642-7439)

Kong Yanlong (Orcid ID: 0000-0002-6414-6266)

Variability of isotope composition of precipitation in the Southeastern Tibetan Plateau from the synoptic to seasonal time scale

Xiaoyi Shi[1,2,4*], Camille Risi[3], Tao Pu[4], Jean-Lionel Lacour[5], Yanlong Kong[6], Ke Wang[6], Yuanqing He[1,4], Dunsheng Xia[1]

[1] MOE Key Laboratory of West China's Environmental System, College of Earth and Environmental Sciences, Lanzhou University, Lanzhou, China

[2] Laboratoire de Météorologie Dynamique, IPSL, Sorbonne Université, Paris, France

[3] Laboratoire de Météorologie Dynamique, IPSL, CNRS, Sorbonne Université, Paris, France

[4] State Key Laboratory of Cryospheric Sciences, Northwest Institute of Eco-environment and Resources, Chinese Academy of Sciences, Lanzhou, China

[5] Institute of Earth Sciences, University of Iceland, Reykjavik, Iceland

[6] Institute of Geology and Geophysics, Chinese Academy of Sciences, Beijing, China

Corresponding author: Xiaoyi Shi (shixysarina@163.com)

Key Points:

- Seasonal isotopic variations are driven both by processes along air mass trajectories and local processes
- Isotopic variations at shorter time scales are driven by local processes
- General circulation models miss the effect of local processes at shorter time scales

This article has been accepted for publication and undergone full peer review but has not been through the copyediting, typesetting, pagination and proofreading process which may lead to differences between this version and the Version of Record. Please cite this article as doi: 10.1029/2019JD031751

Abstract

Daily precipitation samples were collected at 4 sites in Mount Yulong and Mount Meili regions of southeastern TP and analyzed for isotopic composition. Combined with water vapor isotopic composition derived from satellites data (IASI, TES and GOSAT), the factors controlling the variability in the isotopic composition of precipitation are investigated at the synoptic, intra-seasonal and seasonal time scales. At the seasonal scale, the isotope composition in precipitation is controlled by processes along air mass trajectories affecting the water vapor at the large scale (>200km), especially upstream deep convection and air mass origin, and by local processes transforming the large-scale water vapor isotopic composition into the precipitation composition, especially rain evaporation and local circulation. At the intra-seasonal and synoptic scales, the isotope composition in precipitation is mainly controlled by these local processes. The shorter the time scale of isotopic variations, the smaller the spatial imprint of these variations. The fact that different factors controlling the isotopic variability at different time scales calls for caution when applying relationships observed at these time scales to interpret isotopic variations at paleoclimatic time scales. While general circulation models successfully capture the isotopic variability and its controlling factors at the seasonal scale, it fails to simulate them at shorter time scales, because it fails to simulate the local processes.

Plain Language Summary

Water molecules can be light (one oxygen atom and two hydrogen atoms) or heavy (one hydrogen atom is replaced by a deuterium atom). These different molecules are called water isotopes. The isotopic composition of precipitation, when recorded in ice cores, can provide information about past climate. In southeastern TP ice cores, the isotopic records have been interpreted as reflecting past variations in temperature, or as reflecting past variations in monsoon strength. This illustrates that we need to better understand what processes control the isotopic composition of precipitation. We investigate the processes at the seasonal (>1 month), intra-seasonal (10-30 days) and synoptic (<10 days) time scales. We use precipitation samples collected in the southeastern TP, and satellite retrievals of water vapor isotope. We show that storm activity along air mass trajectories is an important factor controlling isotopic variations at the seasonal scale. But local processes, such as the evaporation of rain drops or local winds, are also important, especially at shorter time scales. The fact that the processes controlling the isotopic composition of precipitation depend on the time scale calls for caution when applying the factors observed in present-day variability to interpret isotopic ice core records at very long time scales.

1 Introduction

The Tibetan Plateau (TP), a vast area with an average altitude above 4000 m, encompasses the largest number of glaciers outside the Polar Regions (Yao et al., 2012). With its monsoonal precipitation and glacier melt, it is also considered as a water tower for surrounding regions where billions of people live. Stable isotopes in precipitation provide integrated information on climate and water cycle processes (Galewsky et al., 2016). Understanding what controls the isotopic composition of precipitation in the TP region is necessary for several applications. First, the TP contains a large number of glaciers whose isotopic composition provides a unique window into past climatic variations (Thompson et al., 1990; Yao et al., 1997a; Thompson et al., 2000a). However, the interpretation of past precipitation isotopic variations in the TP is debated, with isotopic variations used as a proxy for temperature (Thompson et al., 1990; Yao et al., 1996, 1997a, 1997b; Thompson et al., 2000b; Yang et al., 2007) or precipitation associated with the strength of the Indian monsoon (Thompson et al., 2000a; Morill et al., 2006; Kaspari et al., 2007; Liu et al., 2007). This calls for a better understanding of the physical mechanisms controlling the isotopic composition of precipitation in the TP region. Second, the isotopic composition of precipitation may provide useful information on water cycle processes in a perspective of water resource management. For example, the isotopic variability of precipitation at short time scales needs to be understood when using isotope-based hydrograph separation to identify the different contributions to runoff and streamflow, or when using isotope-based methods to understand groundwater recharge processes (Pu et al., 2017; Cui et al., 2015; Wang et al., 2018; Kong et al., 2019a). Third, isotopic records of precipitation are used for paleo-altitude reconstructions of the TP (Rowley and Currie, 2006; Rowley, 2007a; Rowley and Garzione, 2017b), based on the observed depletion of precipitation with altitude at present (Dansgaard, 1964). However, recent studies have challenged this approach, arguing that in ancient times, a different combination of dynamical and hydrological processes, in particular convective processes, may lead to an altered relationship between precipitation isotopic composition (Ehlers and Poulsen, 2009; Poulsen and Jeffery, 2011; Shen and Poulsen, 2019), and even a reversed isotopic lapse rate (Botsyun et al., 2019). Therefore, testing our understanding of processes controlling the isotopic composition of precipitation is crucial for more robust paleo-elevation estimates.

In this context, many studies have aimed at better understanding the isotopic composition variability in the TP precipitation at different time scales, from daily to inter-annual time scales. To do so, they have collected precipitation samples and analyzed their isotopic composition. Collectively, these studies showed that in the southern part of the TP, which is affected by the Indian monsoon circulation, especially in summer, deep convection upstream air mass trajectories is the dominant factor (Ishizaki et al., 2012; Gao et al., 2013; Cai et al., 2016, 2017, 2018, 2019; synthesis in Table S1). In the northern part of the TP, which is affected by the westerlies especially during winter, local temperature is the dominant factor (Table S1, e.g. Yao et al., 2013; Yu et al., 2016c). Recent studies also demonstrate that the origin of air masses, depending on whether the moisture comes from the monsoon flow or the westerlies, is a critical factor (Table S1, e.g. Tian et al., 2007, 2008; Yu et al., 2008, 2014; Kong et al., 2019b).

In this study, we present daily precipitation samples and their isotopic composition in the southeastern TP, in Mount Yulong (at Lijiang) and Mount Meili regions (Fig. 1). The region is located at the convergence of air masses between the westerlies and monsoon flows from the Bay of Bengal and the South China Sea (Fig. 1a). We investigate what controls the observed isotopic variability at the synoptic to seasonal time scale. Since our observations cover less than two years, the isotopic variability at the inter-annual time scale, which has already been analyzed in other studies (e.g. Ishizaki et al., 2012; Tan, 2014; Cai and Tian, 2016; Cai et al., 2017, 2019; Shao et al., 2017; Wang et al., 2020), is beyond the scope of this study. Compared to previous studies, our analysis goes further in testing the hypotheses on the physical mechanisms responsible for isotopic variations. First, we make use of existing satellite retrievals of water vapor and its isotopic composition to quantify the relative contributions from processes acting on the water vapor at the large-scale (here we define the "large-scale" as larger than the typical size of a general circulation model, e.g. 200 km), and local processes transforming the large-scale water vapor isotopic composition into the precipitation composition on the other hand. The satellite retrievals also allow us to gather a spatial view of isotopic variations and to assess the spatial coherence of the isotopic variability, which gives complementary information on the processes at play. Second, we filter the isotopic time series to isolate the isotopic variability at different time scales: synoptic, intra-seasonal and seasonal.

Isotope-enabled general circulation models are often used to help understand processes controlling the isotopic variability in precipitation (Risi et al., 2010a; He et al., 2015). To what extent are the different contributions to the δ^2H in precipitation (δ^2H_p) variability over the TP caught by the models? Does it depend on the time scale? Can these results shed some new light on the reasons for the difficulty of models to simulate the isotopic variability over the TP (e.g. Yao et al., 2013)? With this aim, we compare the observed isotopic variations to those simulated by several isotope-enabled general circulation models.

2 Material and methods

2.1 Material

2.1.1 Study area

Located in the southernmost of Hengduan Mountains Range, Mount Yulong (27º10'-27º40' N, 100°9'-100°20' E) with the peak 5 596 m a.s.l. is a typical monsoonal temperate glacier region in China (Fig. 1a). Lijiang basin (26. 86° N, 100. 25° E, 2393 m a.s.l.) is just only 25 km south from Mount Yulong (Fig. 1b). The region is characterized by a typical monsoon climate. The south Asian/Indian monsoon results in abundant rains during the wet season (from May/June to October) with an average annual precipitation of 956.2 mm from 1951 to 2013. Monsoon winds are typically from the South, bringing water vapor from the Bay of Bengal (blue arrow in Fig. 1a) or from the South China Sea (green arrow in Fig. 1a). In contrast, less precipitation occurs in the dry season (from November to the next April) because of the dry and warm air brought by the south branch of the westerly (Pu et al., 2017, yellow arrow in Fig. 1a) with an average temperature of 12.8℃, and an average annual relative humidity of 63% (Shi et al., 2017).

To assess the spatial coherence of isotopic variability in precipitation at different time scales, we also collected daily precipitation samples at 3 sites in Mount Meili (28°33′-28°41′ N, 98°30′-98°40′ E, 6740 m a.s.l.), which is located around 210 km northwest of Mount Yulong and has similar climatic characteristics (Fig. 1c). The 3 sampling sites are Mingyong (28.47°, 98.79° E, 2306 m, MY), Taizimiao (28.46° N, 98.76° E, 2937 m, TZ) and Lianhuasi (28.46° N, 98.76° E, 3243 m, LH), respectively.

2.1.2 Sampling and isotopic analysis

Precipitation was sampled at the daily scale at 4 observation stations (Fig. 1). At Lijiang, precipitation was sampled from 19, March 2017 to 20, August 2018 (Fig. 2a). To assess the spatial coherence of the observed δ^2H variability, precipitation was sampled at three other stations located at different altitudes near Mount Meili, from 26, June 2017 to 31, July 2018 (MY), from 8, August 2017 to 1, August, 2018 (TZ), and from 16, July, 2017 to 1, August, 2018 (LH), respectively (Fig. 2b-d). We make no attempt to assign values into days without precipitation.

To be consistent with the time period of δ^2H in water vapor retrieved from Infrared Atmospheric Sounding Interferometer (see section 2.1.3), only the precipitation data in 2017 at Lijiang were analyzed in this study. This leaves us with 76 days where precipitation isotopic composition is analyzed. When assessing the spatial coherence of the observed δ^2H variability, and for this purpose only, the precipitation data for the whole sampling period of the 4 stations are used, so as to maximize the common periods between the four stations.

All precipitation samples were analyzed with respect to VSMOW at the Key Laboratory of Western China's Environmental Systems (Ministry of Education), Lanzhou University, using a liquid water isotope analyzer (Picarro L2130-i). All $^2H/^1H$ ratios were expressed in δ-notation, with the precision of 0.5‰ for δ^2H.

2.1.3 Water vapor isotopic retrievals by satellite

The precipitation forms locally from water vapor, which records an integrated history of phase change processes along its trajectories. Therefore, it is instructive to separate the isotopic variability observed in precipitation into the isotopic variability in water vapor on the one hand, and the isotopic difference between water vapor and precipitation on the other hand. We thus need the isotopic composition of the water vapor. With this aim, we use isotopic retrievals from three different satellites.

We use δ^2H retrievals from Infrared Atmospheric Sounding Interferometer (IASI, Lacour et al., 2012, 2015, 2018), which is currently the remote sensor with the best spatio-temporal sampling capabilities for δ^2H retrieval. Each location is sampled twice daily, allowing the δ^2H variability in the vapor to be resolved at the synoptic scale. The horizontal footprint of IASI data is 12 km. Full tropospheric profiles are retrieved, but with very limited vertical resolution. We use δ^2H retrievals at 5 km above ground level, close to the level of maximum

sensitivity of the retrievals. Since the IASI retrievals are very computationally expensive, retrievals were computed only for a restricted geographical domain (20-30º N, 94-106º E) for the year 2017.

To put the isotopic variations into a broader regional context, we use the δ^2H retrievals from Tropospheric Emission Spectrometer (TES, Worden et al., 2006, 2007) and Greenhouse gases Observing Satellite (GOSAT, Frankenberg et al., 2013). For TES, we use the optimized version that allows to retrieve vertical profiles with degrees of freedom spread throughout the troposphere (Worden et al., 2012). For consistency with IASI, we also use retrievals at 5 km above ground level. For GOSAT, we use the column-integrated δ^2H, because no vertical profiles can be retrieved from this technique. Since most of the total-column vapor is in the lower troposphere, column-integrated δ^2H is strongly weighted towards the δ^2H of the boundary layer.

IASI, TES and GOSAT products are from clear-sky only. We select only profiles that reach several quality criteria. Specifically, for GOSAT measurements, we select measurements that met following quality criteria (Risi et al., 2013): no cloud; retrieved precipitable water (W) agrees within 30% with ECMWF reanalysis; errors on retrieved W and column-integrated HDO are lower than 15% (Frankenberg et al., 2013); retrieval χ^2 is lower than 0.3; retrieved δ^2H is within -900‰ and 1000‰ to exclude a few obviously anomalous values. For TES, we select only TES measurements with a valid quality flag and a degree of freedom of the signal (DOFS) greater than 0.5. All these conditions reduce the spatio-temporal sampling. The TES measurements, retrieval methods and uncertainties are described in earlier studies (Worden et al., 2006, 2007; Risi et al., 2010a). Satellite products usually lack absolute calibration, and effectively show large offsets between each other (Risi et al., 2012). When interpreting TES, GOSAT and IASI retrievals, we only focus on temporal variability rather than on absolute values.

TES and GOSAT have a low spatio-temporal sampling, and were not available anymore in 2017. Therefore, we use these products to analyze the seasonal variations only, using multi-year-mean monthly values to describe the seasonal cycle. Years are 2004-2007 (corresponding to the period when the sampling frequency was maximum) for TES and 2009-2011 for GOSAT.

We acknowledge that the seasonal cycle of the isotopic composition may vary from year to year, in association with inter-annual variability modes such as El Nino Southern Oscillation (ENSO). However, for water isotopes, inter-annual variations are generally smaller than seasonal variations. We checked this both in precipitation and in the water vapor. For precipitation, we used the Tibetan Network for Isotopes in Precipitation (TNIP) data at Lhasa which covers 13 years from 1994 to 2006. The multi-annual-mean seasonality in $\delta^{18}O$ (no observed δ^2H data), quantified as the July-August minus March-April $\delta^{18}O$ difference, is -12.1‰, whereas the inter-annual standard deviation of the $\delta^{18}O$ seasonality is 6.9 ‰. This confirms that inter-annual variations are smaller than seasonal variations. For the water vapor, we assessed the robustness of the δ^2H seasonality using 8 years of TES observations (2004-2011). Over most of the TP region and China, the multi-annual-mean seasonality in δ^2H is larger than the inter-annual standard deviation of the seasonality (Fig. S1), including Lijiang with a factor 2. Therefore, this gives us confidence that the seasonal variations that we analyze with the TES and GOSAT datasets are robust and are informative even though the time periods

are different. Finally, note that the year 2017, when our precipitation was sampled at Lijiang and Mount Meili stations, was an ENSO-neutral year at the global scale (Ramirez and Briones, 2017).

We will show in the results section that at the seasonal scale, TES, GOSAT and IASI give results that are very smooth and spatially coherent. Results are noisier and less spatially coherent for IASI at the intra-seasonal and synoptic time scales. To assess to what extent this noise and weaker spatial coherence are physical and not artifacts due to errors, we performed an extensive error analysis detailed in Appendix 1, including errors associated with the instrument sensitivity, random errors, and sampling biases in time and in space.

2.1.4 Meteorological observations

To look at the relationships between observed δ^2H in precipitation and local meteorological conditions, surface air temperature, precipitation amount and relative humidity data were used (Fig. 3b-d).

To assess the effect of the origin of air masses, we use wind direction at 15 m corresponding the daily maximum wind speed at Lijiang from the China Meteorological Data Service Center (CMDC). The wind direction, binned into 16 directions, was converted into direction in degrees between 0 and 360°, where the 0°-360° discontinuity corresponds to the North (Fig. 3e). The wind rose shows that the wind most often blows from the South-East or from the West (Fig. S2). The fact that the wind direction varies non-monotonically from 360° to 0° when going from North-Westerly to North-Easterly could be a problem when calculating correlations, because correlation analysis is designed to assess the relationships between monotonically varying variables. In our case, the fact that northerly wind is scarce prevents issues associated with this 360°-0° discontinuity.

To explore the influence of upstream convection on the δ^2H in precipitation, daily precipitation data from Tropical Rainfall Measuring Mission (TRMM, Huffman et al., 2007) is available for the sampling period with the spatial resolutions of 0.25°× 0.25°.

To access the influence of Indian monsoon, the Indian Summer Monsoon (ISM) index is also defined with the 850hPa zonal winds averaged over the southern Arabian Sea region (5°-15° N, 40°-80º E) minus that averaged over the northern region (20º-30º N, 70º-90º E) (Fig. 3f), reflecting the large-scale rainfall variability of the Indian summer monsoon (Wang et al., 2009; Gao et al., 2018). The 850hpa zonal wind data at 2.5°× 2.5° resolution are obtained from the NCAR/NCEP reanalysis data (Kalnay et al., 1996).

2.1.5 Model simulations

To assess the ability of isotope-enabled general circulation models (GCMs) to capture the seasonal isotopic variability at Lijiang, we use the outputs of nine simulations from seven isotope-enabled GCMs archived by Stable Water Isotope Intercomparison Group, Phase 2 (SWING2, Table S2) (Risi et al., 2012). The SWING2 simulations do not all have the same setup: some simulations are free-running and forced by observed sea surface conditions, whereas in others the horizontal winds are nudged towards reanalysis data to ensure a more realistic simulation of the large-scale circulation (Table S2). In addition, the period of the

simulations does not correspond to the data period. Therefore, the simulation set-up in available SWING2 simulations is not perfect for this data-model comparison. However, the seasonal variability that we investigate using these simulations is much larger than the year-to-year variability, as explained in section 2.1.3.

Only monthly outputs are archived in the context of the SWING2 project. Therefore, for outputs at the shorter time scale, we used simulations using the LMDZ5A version of LMDZ (Laboratoire de Météorologie Dynamique Zoom), which is the atmospheric component of the IPSL-CM5A coupled model (Dufresne et al., 2013) that took part in CMIP5 (Coupled Model Intercomparison Project). This version is very close to LMDZ4 (Hourdin et al., 2006). Water isotopes are implemented with the same way as in its predecessor LMDZ4 (Risi et al., 2010a). The simulation is forced by observed monthly sea-surface conditions and the winds are nudged towards the 6-hourly winds from the ECMWF operation analyses (Uppala et al., 2005). Such a simulation has already been described and extensively validated for isotopic variables in both precipitation and water vapor (Risi et al., 2010a; Risi et al., 2012). We use the outputs for the year 2017 to compare with in situ measurements at Lijiang.

2.2 Methods

2.2.1 δ^2H filtering

Because the daily δ^2H in precipitation combines the variability at different time scales, we decompose the isotopic changes into 3 different time scales: “seasonal”, “intra-seasonal” and “synoptic” scales (eg, Fig. 3a at Lijiang).

To do so, we filter the daily δ^2H time series by applying a moving average with time constants of 30 days and 10 days. The moving average acts as a low-pass filter. We note δ^2H_{10} and δ^2H_{30} as the 10 days and 30 days filtered δ^2H time series respectively. The raw daily δ^2H time series is decomposed into seasonal (δ^2H_{seaso}), intra-seasonal (δ^2H_{intra}) and synoptic (δ^2H_{synop}) components:

$$\delta^2H = \delta^2H_{seaso} + \delta^2H_{intra} + \delta^2H_{synop}$$

where δ^2H_{seaso} is calculated as $\delta^2H_{seaso} = \delta^2H_{30}$ and represents the “seasonal” part of the δ^2H variability, δ^2H_{intra} is calculated as $\delta^2H_{intra} = \delta^2H_{10} - \delta^2H_{30}$ and represents the “intra-seasonal” part, and δ^2H_{synop} is calculated as $\delta^2H_{synop} = \delta^2H - \delta^2H_{10}$ and represents the “synoptic” part (Fig. 3a).

All other time series (eg. Fig. 3b-f, temperature, relative humidity, wind direction…) can be filtered in the same way.

2.2.2 Precipitation δ^2H decomposition

The goal is to decompose the daily-mean isotopic variability observed in the precipitation into the contribution from different processes (e.g, Botsyun et al., 2016) as illustrated in Fig. 4. We exploit the fact that we have water vapor δ^2H observations from IASI for the same period as our precipitation δ^2H, i.e. for the year 2017. First, we write the

precipitation isotopic ratio (R_p) as the isotopic ratio in equilibrium with the vapor ($\alpha \cdot R_{vLS}$) plus a residual:

$$R_p = \alpha \cdot R_{vLS} + \left(R_p - \alpha \cdot R_{vLS}\right) \quad (1)$$

α is the equilibrium fractionation coefficient that depends on temperature (Majoube, 1971) .

R_{vLS} is estimated from IASI retrievals at 5 km altitude. Every day, we average allprofiles in a 3.6°x2.5° grid box. In average, there are 26.5 profiles per day in the Lijiang grid box. Therefore, R_{vLS} represents the isotopic composition of the vapor at the large scale, hence the subscript "LS".

We define

$$R_{veq} = R_p/\alpha \quad (2)$$

where R_{veq} is the isotopic composition of vapor under precipitation - vapor equilibrium.

We further decompose α into its temporal mean over the full sampling period ($\overline{\alpha}$) plus its anomaly (α'):

$$\alpha = \overline{\alpha} + \alpha' \quad (3)$$

Rearranging equations yields:

$$R_p = \alpha' \cdot R_{veq} + \overline{\alpha} \cdot R_{vLS} + \overline{\alpha} \cdot \left(R_{veq} - R_{vLS}\right) \quad (4)$$

In delta notation, this yields:

$$\delta^2 H_p = \frac{\alpha' \cdot R_{veq}}{R_{smow}} \cdot 1000 + \left(\frac{\overline{\alpha} \cdot R_{vLS}}{R_{smow}} - 1\right) \cdot 1000 + \frac{\overline{\alpha} \cdot \left(R_{veq} - R_{vLS}\right)}{R_{smow}} \cdot 1000 \quad (5)$$

The first term on the right-hand side represents the effect of variations in the precipitation-vapor equilibrium fractionation factor (Fig. 4, black dashed circle). The second term represents the effect of variations in water vapor δ^2H at the large-scale. These variations integrate all processes along air mass trajectories (Fig. 4, blue dashed square). The third term (Fig. 4, magenta dashed square) represents a combination of precipitation-vapor disequilibrium effects (due to variations in condensation altitude or post-condensation processes such as rain evaporation), variations in the vertical gradients between the surface (where the precipitation achieves its last equilibration, e.g. Graf et al., 2019) and 5 km (where the water vapor δ^2H is observed by IASI) and small-scale variations in water vapor δ^2H (leading to difference between the water vapor δ^2H observed by IASI and that with which the precipitation locally equilibrates).

This decomposition can be applied on raw time series, or on filtered time series (section 2.2.1). In any case, all variables in Eq. (5) are filtered at the same time scale and following the same procedure.

2.2.3 Back trajectory analysis and cumulated precipitation along trajectories

Many previous studies have shown the relationship between δ^2H_p and precipitation upstream air mass trajectories (Vimeux et al., 2005; Risi et al., 2008b; Gao et al., 2013; He et al., 2015). To assess this effect, we compute daily back trajectories from Lijiang based on a 2D trajectory algorithm (Vimeux et al., 2005) and ECMWF ReAnalysis - Interim (ERA-I) (Dee et al., 2011) 6-hourly meridional and zonal wind fields. Each day, a trajectory is calculated with time steps every 6 hours backward in time, up to 7 days.

TRMM precipitation was cumulated along the n previous days along each trajectory, n varying from 1 to 7. This yields a time series of cumulated precipitation along trajectories.

3 Results

3.1 δ^2H time series and relationship with local meteorological variables

Daily δ^2H_p vary greatly from -173.5‰ to 2.4‰ during the sampling period, with a weighted-average value of -99.5‰ (Fig. 2a). Precipitation isotope is enriched from November to May, corresponding to the non-monsoon season, and depleted from June to October, corresponding to the Indian monsoon season. This is consistent with the previous studies in the southeastern TP (Yu et al., 2016b; Pang et al., 2006; Pu et al., 2017).

In order to further asses what controls the variability of precipitation δ^2H at different time scales (seasonal, intra-seasonal and synoptic scale), we analyze the relationships between δ^2H_p and local meteorological factors (eg, temperature, precipitation amount, relative humidity and wind direction) (Table 1). In particular, the local temperature and precipitation amount are often explored as possible factors controlling the δ^2H_p in the southern TP (Pang et al., 2006; Yao et al., 2013; Yu et al., 2016a). The intensity of the monsoon is also often cited (Wang et al., 2009; Gao et al., 2018), quantified here by the ISM. Note that when calculating correlations between two variables, regardless of whether they are isotopic or metrological variables, we always ensure that these two variables cover the same time period and that the smoothing time scale is the same.

At all the time scales, the correlation between δ^2H_p and local precipitation is weak ($r = -0.26$, $p < 0.05$ at the seasonal scale, $r = -0.27$, $p < 0.05$ at the synoptic scale), discarding the local amount effect as a major control of the δ^2H_p variations. In contrast, the strong correlation between δ^2H_p and the ISM ($r = -0.75$, $p < 0.01$ at the seasonal scale, $r = -0.41$, $p < 0.01$ at the intra-seasonal scale) suggests that the "amount effect" upstream air mass trajectories, associated with deep convection along trajectories, is an important factor. This is consistent with previous studies (Gao et al., 2013; He et al., 2015; Dong et al., 2016) that showed that local precipitation is not sufficient to explain the δ^2H_p variability in the southern TP, and that upstream deep convection is a more important factor (section 3.3).

The correlation between δ^2H_p and local temperature is very significant at the seasonal scale ($r = -0.75$, $p < 0.01$, Table 1). Yet, in a causal relationship associated with the distillation

of air masses, we would expect δ^2H_p to increase with temperature (Dansgaard et al 1964). We notice that this correlation is the same as between δ^2H_p and the ISM, and that temperature and the ISM are strongly correlated ($r = 0.97$, $p<0.01$, Table S3). Therefore, the link between δ^2H_p and temperature is probably simply a consequence of the link between δ^2H_p and the ISM. The correlation between δ^2H_p and local temperature is also significant, though weaker, at the synoptic scale ($r=0.33$, $p<0.05$). Such a positive correlation could be due to the distillation of air masses, or to the correlation of both δ^2H_p and temperature with the local meteorological situation.

The meteorological variable that correlates the most strongly with δ^2H_p is local wind direction ($r=0.94$, $p<0.01$ at the seasonal scale, $r=0.60$, $p<0.01$ at the intra-seasonal scale). Precipitation δ^2H is more depleted during the monsoon season when air comes from the South, and more enriched when the air comes from the West. This is consistent with the effect of moisture origin highlighted in several previous studies (Tian et al., 2007, 2008; Yu et al., 2008, 2014; Kong et al., 2019b). However, the local wind direction observed at Lijiang is more representative of the local circulation or meteorological situation than the large-scale circulation. The correlations between local wind direction and the direction of air mass trajectories (e.g. quantified as the direction of the vector connecting Lijiang from the trajectory location 3 days before its arrival, hereafter "trajectory direction") are weak and significant only at the seasonal scale ($r = 0.69$, $p<0.01$, Table S3). The correlations between δ^2H_p and trajectory direction are also significant, though weaker ($r = 0.70$, $p<0.01$ at the seasonal scale, $r=0.53$, $p=0.01$ at the intra-seasonal scale, Table 1). Therefore, both local wind direction associated with local circulation and meteorological situation, and to a lesser extent trajectory direction associated with the large-scale circulation and origin of air masses, emerge as important factors.

The second meteorological variable that correlates the most strongly with δ^2H_p is relative humidity ($r =-0.80$, $p<0.01$ at the seasonal scale, $r=-0.41$, $p<0.01$ at the intra-seasonal scale). The lower correlation between relative humidity and the ISM indicates that this cannot be a simple consequence of the link between δ^2H_p and the ISM. Relative humidity can impact δ^2H_p through two main mechanisms: first, low relative humidity is associated with stronger subsidence that bring depleted water vapor downward (Frankenberg et al., 2009, Galewsky and Hurley, 2010). This would lead to a positive correlation opposite to what we observe. Second, low relative humidity drives stronger rain evaporation that enriches δ^2H_p. This probably leads to the negative correlation that we observe. Finally, it is also possible that both relative humidity and δ^2H_p independently respond to the seasonal climate pattern and seasonal moisture transport, in a way that is slightly different from the ISM. More generally, this correlation analysis is useful to hypothesize what processes drive the δ^2H_p variability. However, a correlation does not necessarily mean a causal relationship. To better understand whether rain evaporation is a major factor controlling the δ^2H_p seasonality, we turn to our decomposition method.

3.2 Decomposition of the variability in δ^2H in precipitation

To better understand what process drive the precipitation δ^2H variability, the raw and filtered time series are decomposed into 3 contributions as explained in section 2.2.2 and illustrated in Fig. 4. For example, Fig. 5 shows the raw precipitation δ^2H time series and its 3

contributions. We can check that the sum of the 3 contributions (Fig. 5, black dashed line) yields the initial raw precipitation time series (Fig. 5, magenta). We can see that the first contribution $\alpha' \cdot R_{veq}$ (Fig. 5, black), which represents the effect of temperature variations on precipitation-vapor equilibrium fractionation coefficient, is very small. It can be neglected. The second contribution $\overline{\alpha} \cdot R_{vLS}$, and the third contribution $\overline{\alpha} \cdot \left(R_{veq} - R_{vLS}\right)$ show large fluctuations, and their impact on the δ^2H variability at different time scales can be quantified by the correlation analysis that follows. Quantitatively, Table 2 summarizes the correlation coefficients and slopes of the three different contributions as a function of δ^2H_p at different time scales.

At the seasonal scale, δ^2H_p is significantly correlated with the third contribution $\overline{\alpha} \cdot \left(R_{veq} - R_{vLS}\right)$ (r=0.97, p<0.01). The slope indicates that it contributes to 69% of the δ^2H_p variations (Table 2). This suggests that processes transforming the δ^2H_{vLS} variability into the δ^2H_p variability are the main drivers of seasonal variation in δ^2H_p at Lijiang. This is consistent with section 3.1 that suggested a key role for local processes, especially local circulation and rain evaporation. The role of local circulation is further supported by the correlation between the third contribution and local wind direction (r = 0.97, p < 0.01). The local circulation could drive small-scale vertical and horizontal heterogeneities in water vapor δ^2H relatively to δ^2H_{vLS}. The role of rain evaporation is also further supported by the correlation between the third contribution and relative humidity (r = -0.91, p < 0.01): as the air is drier, the precipitation evaporates more efficiently as it falls and gets more enriched relatively to δ^2H_{vLS}.

Another prominent correlation at the seasonal scale is between δ^2H_p and the second contribution $\overline{\alpha} \cdot R_{vLS}$ (r=0.81, p<0.01). The slope indicates that it contributes to 27% of the δ^2H_p variations (Table 2). This probably reflects convective processes along air mass trajectories (section 3.3). This could also include an effect of the moisture origin: the second contribution also correlates significantly with local wind direction (r=0.62, p<0.01), which at the seasonal scale reflects both local and large-scale circulation (section 3.1, Table S3).

At the intra-seasonal scale, δ^2H_p is significantly correlated with the third contribution (r = 0.90, p<0.01). This indicates that processes transforming the δ^2H_{vLS} variability into the δ^2H_p variability are the main drivers, contributing to 115 % of δ^2H_p variations. This local contribution may reflect both the effect of rain evaporation (r=-0.33, p<0.01 with relative humidity) and of local circulation (r=0.79, p<0.01). The fact that this contribution exceeds 100 % indicates that it is counter-balanced by another processes. It means that without the other counter-balancing process, the δ^2H_p variability would be greater than observed. This counter-balancing process is represented by the second contribution. Indeed, δ^2H_p is negatively correlated with the second contribution, indicating that processes along trajectories are not drivers. Rather, these processes blur or dampen the δ^2H_p variability.

At the synoptic scale, processes transforming the δ^2H_{vLS} variability into the δ^2H_p variability dominate (r=0.46, p<0.01), contributing to 68% of the synoptic variability in δ^2H_p. Since no significant correlation between the third contribution and relative humidity can be

detected, we can discard a significant effect of rain evaporation. No significant correlation between the third contribution and local wind speed can be detected either, discarding an effect of local circulation. Small-scale vertical and horizontal heterogeneities in water vapor δ^2H, associated with local meteorological conditions, could be the main drivers of this contribution.

Could errors in IASI affect our result that processes transforming δ^2H_{vLS} into δ^2H_p emerge as the most important contribution at all time scales? Actually, IASI errors tend to lower the contribution of this contribution (Appendix 1). Therefore, in reality we may expect an even larger contribution of these processes.

3.3 Relationship with upstream convection

To test the hypothesis that at the seasonal scale deep convection upstream air mass trajectories is also a key driver of δ^2H_p variations, daily TRMM precipitation is cumulated along the n previous days along each air mass trajectories. The temporal correlation between δ^2H_p and δ^2H_{vLS} and cumulated precipitation amount is shown as a function of n (Fig. 6).

At the seasonal scale, δ^2H_p is significantly anti-correlated with the cumulated precipitation amount from 1 to 3 days preceding the rainy event. The strongest negative correlation is obtained for n = 2 days ($r = -0.89$, $p < 0.01$). δ^2H_{vLS} exhibits a similar pattern, which is remarkable given that precipitation and water vapor δ^2H are from completely independent sources of data. This result is consistent with previous studies highlighting the important role of deep convection along air mass trajectories in the TP region (Table S1), and in other monsoon regions of the world (Vimeux et al., 2005; Risi et al., 2008a, b; Vimeux et al., 2011; Tremoy et al., 2012).

Air mass trajectories are associated with the monsoon flow in the lower troposphere. The mechanisms by which deep convection depletes the lower tropospheric water vapor along the air mass trajectories have already been documented in previous observational and modeling studies. First, convective or meso-scale downdrafts bring depleted water vapor from the free troposphere downward (Risi et al., 2008b, 2010a; Kurita et al., 2013). Second, rain evaporation in moist conditions and diffusive exchanges between the rain and vapor deplete the water vapor (Lawrence et al., 2004; Worden et al., 2007; Field et al., 2010; Lacour et al., 2018).

At the intra-seasonal and synoptic scales, there is no significant anti-correlation with the cumulated precipitation. This is consistent with the result of the previous section suggesting that at these time scales, the observed variability is not driven by processes affecting the large-scale water vapor, but rather by local processes transforming the large-scale water vapor variability into the precipitation variability. However, at the intra-seasonal scale, we observe a significantly positive correlation between water vapor δ^2H and cumulated precipitation for all lags. We do not know how to interpret this correlation. We can't find any physical mechanisms that would lead to such a correlation.

3.4 Spatial scale of isotopic variability in precipitation and vapor

To test whether the local processes produced the short-term variation in precipitation and vapor δ^2H, we use three different datasets. 1) TES and GOSAT datasets are used to show

the seasonal difference of δ^2H in vapor at the scale of China and nearby countries (Fig. 7); 2) IASI daily output of δ^2H in vapor is used to show the spatial coherence of water vapor δ^2H variations from the seasonal to synoptic scale; 3) Observed daily precipitation isotope in Mount Yulong and Mount Meili are used to access the spatial scale of isotopic variability.

The TES and GOSAT data show that the seasonal variations observed at Lijiang, with more depleted precipitation in the monsoon season (July-August) than before the monsoon onset (March-April), are also observed in a wide region from about 18°N to 30°N and 85°E to 120°E (Fig. 7). The deep convection associated with the Indian monsoon occurs over a wide region, thus impacting the water vapor δ^2H over a wide region as well.

The IASI observations allow us to assess the spatial imprint of the δ^2H variability at the seasonal to synoptic scales (Fig. S3). At the seasonal scale, the water vapor δ^2H at Lijiang correlates significantly with the water vapor δ^2H everywhere around ($r>0.8$), consistent with the fact that the seasonality of water vapor δ^2H has a very wide spatial imprint. At the intra-seasonal scale, the correlations are significant over a smaller region of a few hundreds of kilometers ($r>0.4$). At the synoptic scale, the correlations become insignificant everywhere ($r<0.4$), consistent with purely local processes controlling the variability.

To further assess the spatial coherence of the δ^2H variability, precipitation δ^2H at Lijiang is compared with that observed at 3 other sites distributed at different altitudes (Fig. 1, section 2.1.1). The correlation for each pair of sites is calculated at different time scales (Table 3). At the seasonal scale, δ^2H_p at Lijiang is strongly correlated with δ^2H_p at the 3 sites at Mount Meili ($r>0.88$, $p<0.01$, Table 3). This is consistent with the large-scale imprint of the seasonal variations.

At the intra-seasonal scale, a robust positive correlation ($p<0.05$) is observed only between δ^2H at Lijiang and TZ in Mount Meili (Table 3). This confirms that the spatial scale of intra-seasonal variations is smaller than for seasonal variations. At the synoptic scale, there is no relationship between Lijiang and the three sites at Mont Meili, supporting the small spatial scale of synoptic variations and thus the importance of local processes.

To summarize, the shorter the time scale of isotopic variations, the smaller the spatial imprint of these variations.

3.5 Comparison with isotope-enabled general circulation models

We have quantified the relative contributions of different processes to the isotopic variability at Lijiang, and have assessed their spatial imprint. To what extent are these different contributions captured by the models?

At the seasonal scale, most models participating in SWING2 capture the seasonal cycle (Fig. 8, Table 4, $r > 0.49$ between observed and simulated δ^2H at Lijiang for each model) because to some extent all models are able to capture the Indian monsoon and the associated depleting effect of deep convection. Qualitatively, the seasonality simulated by SWING2 models shows a large spatial coherence (Fig. S4), consistent with the pattern exhibited by

satellite observations (Fig. 7). The capacity of GCMs to simulate the seasonality of δ^2H further supports the importance of processes that have a large spatial imprint i.e. convection integrated several days along trajectories or air mass origin. However, we note that many models underestimate the seasonal variations observed at Lijiang (Fig 8; Table 4: the slopes of simulated vs observed monthly δ^2H_p are all lower than 1) and more generally in the monsoon domain of the Tibetan Plateau and more generally in the monsoon domain of the Tibetan Plateau (Fig. S4 compared with Fig. 7). This underestimation had already been noticed in previous studies focusing on δ^2H_p in China (Che et al., 2016), and more generally in the monsoon domain of the Tibetan Plateau (Gao et al., 2011). These studies highlight the need for high horizontal resolution to properly simulate the observed δ^2H_p depletion during the monsoon season.

LMDZ results are consistent with those in SWING2 models. LMDZ can capture the seasonal cycle very well ($r = 0.99$, $p < 0.01$; Table 5, Fig. 9a), in spite of a slight underestimation of the amplitude (slope of 0.8). LMDZ also captures the δ^2H_{vLS} seasonal variability observed by IASI, after taking into account the effect of instrument sensitivity ($r=0.74$, $p<0.01$, Fig. 9b, Table 5). The slightly lower correlation coefficient for the vapor can be explained by the different sources of IASI errors, namely random errors and sampling biases (Appendix 1).

We now investigate the driver of the δ^2H_p seasonality in SWING2 models. In all models but HadAM3_free, the main driver of δ^2H_p is the $\overline{\alpha} \cdot R_{vLS}$ contribution, at odds with observations that show a dominance of local processes (section 3.2, Table 2). Most models underestimate the $\overline{\alpha} \cdot (R_{veq} - R_{vLS})$ contribution (Table 4).

The same holds for LMDZ: processes along trajectories dominate in LMDZ (Table 6, 79%) and local processes transforming δ^2H_{vLS} into δ^2H_p are secondary (Table 6, 16%). This is in contrast with observations, which show that processes along trajectories dominate (section 3.2, Table 2). This mismatch cannot be due to errors from IASI (instrument sensitivity, random errors, sampling bias in time and in space). As shown in Table S7, errors in IASI tend to make the contribution of local processes weaker and even negative (Appendix 1, Table S7). Therefore, the mismatch is rather due to model shortcomings.

It is possible that a better horizontal resolution would improve the simulation of local processes transforming δ^2H_{vLS} into δ^2H_p, enhance their contribution, and thus enhance the seasonal amplitude of δ^2H_p in better quantitative agreement with observations. Although LMDZ underestimates the contribution of local processes, it seems to be able to capture the drivers of this contribution. The correlation between $\overline{\alpha} \cdot (R_{veq} - R_v)$ and relative humidity is -0.59, suggesting that in LMDZ, rain evaporation is a major driver of this contribution, consistent with observations (section 3.2).

To evaluate the capacity of GCMs to simulate the δ^2H_p variability at the intra-seasonal and synoptic scales, we use outputs from LMDZ. LMDZ can capture the intra-seasonal variations to some extent (r = 0.67, p<0.01) but underestimates them (slope of 0.56, Table 5). Similarly, it captures the δ^2H_{vLS} variability observed by IASI, after taking into account the effect of instrument sensitivity (r=0.56, p<0.1, Fig. 9b, Table 5). As for the seasonal scale, the slightly lower correlation coefficient for the vapor than for the precipitation can be explained by the different sources of IASI errors (Appendix 1). In contrast, LMDZ fails to capture the variability at the synoptic scale (r = 0.15).

LMDZ overestimate the $\overline{\alpha} \cdot R_{vLS}$ contribution compared observations (Table 6 compared to Table 2): 39 % compared to -21 % at the intra-seasonal scale, and 69 % compared to a non-significant contribution at the synoptic scale. Considering IASI errors does not affect this conclusion (Table S7 compared to Table 6). Conversely, LMDZ underestimates the local processes that are encapsulated in $\overline{\alpha} \cdot \left(R_{veq} - R_{vLS}\right)$: 62 % compared to 115 % at the intra-seasonal scale and 32 % compared to 68 % at the synoptic scale (Table 6 compared to Table 2). Again, considering IASI errors would not change this conclusion (Table S7 compared to Table 8). The difficulty to represent this local contribution may explain the difficulty of LMDZ to capture the intra-seasonal and synoptic δ^2H_p variability. It is possible that the coarse resolution for LMDZ is not sufficient to represent the local processes transforming the δ^2H_{vLS} variability into δ^2H_p variability, for example local circulations or spatial heterogeneities in δ^2H_{vLS} at the small scale.

4 Discussion

4.1 Comparison with factors controlling precipitation δ^2H in previous studies

Both sets of processes (processes along trajectories and local processes) had already been independently highlighted in previous studies. The importance of deep convection upstream trajectories in controlling the δ^2H variations had already been reported in previous studies, both in the southern -TP (e.g. Gao et al., 2013; He et al., 2015) and in other monsoon regions such as South America (Vimeux et al., 2005) and Western Africa (Risi et al., 2008a, 2010c). The importance of rain evaporation had also been pointed in the Southern TP (Ren et al., 2017) and in Western Africa (Risi et al., 2010b). These two processes are known to contribute to the amount effect (Risi et al., 2008b).

In this work, our study proposes a way to quantify the relative importance of these two sets of processes based on observations. At the intra-seasonal and synoptic scales, the dominance of local processes is in contrast with most previous studies that highlighted the effect of deep convection along trajectories at other sites in the Southern TP (e.g. Lhasa: Gao et al., 2013; He et al., 2015) and in other monsoon regions such as South America (Vimeux et al., 2011) or Western Africa (Risi et al., 2008, 2010a; Tremoy et al., 2012). This may be because of the complex terrain and diversity of trajectories in our region of interest. For example, in the Sahel, the terrain is essentially flat, and in South America, the air mass trajectories are less diverse (Vimeux et al., 2005). Our study also highlights the key role of

local circulations, in addition to the role of the large-scale circulation that had been highlighted in previous studies (Tian et al., 2007, 2008; Yu et al., 2008, 2014; Kong et al., 2019b).

4.2. Implications for the use of isotope-enabled models to study isotopic variability in the TP

All GCMs overestimate the effect of processes along trajectories affecting the water vapor composition at the large scale, whereas they underestimate the effect of local processes transforming this large-scale water vapor composition into local precipitation composition. Since local processes are increasingly important at shorter time scales, this may explain the difficulty of GCMs to simulate the δ^2H_p variability at shorter time scales. Insufficient horizontal resolution is a possible candidate for this shortcoming. Thus, to investigate what controls the isotopic variability at the synoptic time scales, an isotope-enabled model with much higher horizontal resolution would probably be needed (e.g. Moore et al., 2014, 2016; Dutsch et al., 2016, 2018).

4.3 Dependence on the time scale and implications for the interpretation of paleoclimate records

At the seasonal scale, the isotopic variation in precipitation and vapor is affected by the integrative effect of convective activity over several days preceding precipitation events, combined with a possible effect of air mass origin, but this is not the case at shorter time scales. This highlights the importance of separating the time scales when investigating the role of deep convection. If analyzing the correlations with the raw time series, we would have been misled to believe that the daily variability in δ^2Hp is not associated with upstream deep convection, whereas in reality the daily variability in $\delta^2 H_p$ at the seasonal scale is also affected by the upstream deep convection.

Our study shows that the factors controlling δ^2H variability strongly depend on the time scale. Therefore, applying our results to interpret paleoclimate records is not obvious. A strong dependence on the time scale was also highlighted by Hu et al., (2019) between the inter-annual to the precessional time scales. Together with our results, this calls for caution when using relationships observed at short time scales to interpret paleoclimate records.

We show that local processes dominate at synoptic to intra-seasonal time scales. At the seasonal time scale, both local processes and processes along trajectories, including upstream deep convection, are important. We can thus hypothesize that processes along trajectories would dominate more and more at longer time scales. Our record is too short to show any results at the longer time scale, but previous studies confirm this hypothesis and have highlighted the dominance of processes along trajectories, especially the origin of air masses at the inter-annual time scale (Hu et al., 2019) and at the precessional and millennial time scales (Tabor et al., 2018) or upstream deep convection associated with ENSO at the inter-annual time scale (Ishizaki et al., 2012; Tan, 2014; Cai et al., 2016, 2017; Shao et al., 2017; Gao et al., 2018) and at the precessional and millennial time scales (Pausata et al., 2011; Lee et al., 2012; Battisti et al., 2014).

We show that the longer the time scale from synoptic to seasonal, the larger the spatial scale of variations recorded in precipitation δ^2H (section 3.4). We may expect this to remain

true at scales even longer. The enhanced spatial coherence of precipitation δ^2H at the inter-annual time scale, and even more at the precessional time scale, was already highlighted in Hu et al. (2019). At the glacial-interglacial time scale, the homogeneity of δ^2H variations recorded in ice cores over tropical mountain regions around the globe is even more remarkable (Thompson et al., 2000b), which suggests that precipitation δ^2H at such long paleo-climatic time scale may record a very large-scale variability, maybe at the tropical scale.

5 Conclusion

We have collected the daily precipitation samples at Lijiang in Mount Yulong region and at 3 sites in the Mount Meili region, and investigated what controls the isotopic variability at the seasonal, intra-seasonal and synoptic time scales based on a decomposition method using water vapor isotopic measurements by satellite.

At the seasonal scale, two kinds of processes control the variability in precipitation δ^2H. First, processes along trajectories, particularly deep convection and the origin of air masses, affect the water vapor composition at the large scale. Second, local processes transform the isotopic variability in the large-scale water vapor into the local variability in the precipitation. These local processes may include small-scale spatial heterogeneities, variations in the vertical isotopic gradient, local circulation, condensation or post-condensation processes. Particularly, rain evaporation and local circulation emerge as important factors. At the seasonal scale, both kinds of processes have a large-scale spatial imprint.

At the intra-seasonal and synoptic scales, local processes dominate. The shorter the time scale of isotopic variations, the smaller the spatial imprint of these variations. We thus highlight the dependence of the isotopic drivers to the time scale of variability. Consequently, we emphasize the need to filter the time series to separate the different time scales. If we had analyzed the raw daily scale only, we would have been misled to over-estimate the importance of deep convection upstream trajectories at short time scales, and to underestimate its importance at the seasonal scale.

Isotope-enabled general circulation models can qualitatively capture the seasonal variations in δ^2H, but they underestimate the contribution of local processes and overestimate the contribution of processes along trajectories. Local processes that impact the isotopic variability are underestimated at the intra-seasonal and synoptic scale by LMDZ with a coarse resolution, explaining its difficulty to reproduce the observed variations at these time scales.

Appendix 1: Sources of errors in δ^2H retrieved by IASI

The goal is to assess the impact on the results of different sources of errors affecting the IASI observations. We quantify different sources of errors, and the impact of these sources of errors on our results. We cannot compare the results we would get with and without errors in IASI, since the real δ^2H is not known. Therefore, we compare what we would get with and without IASI errors in LMDZ. We note $\delta^2H_{v\_LMDZ}$ the δ^2H_v simulated by LMDZ, and $\delta^2H_{v\_IASI}$ the δ^2H_v observed by IASI.

1.1 Effect of instrument sensitivity

Due to limited instrument sensitivity, the retrieved profiles are smoothed versions of the true profiles. The averaging kernels describe the vertical sensitivity of the retrieval at each level to the true state at each level (Worden et al 2006; Risi et al., 2012). These depend on the atmospheric state. Therefore, part of the δ^2H variability measured by satellites can be attributed to the variability in instrument sensitivity. To quantify this effect, we calculate the water vapor δ^2H that IASI would retrieve if it was flying over the atmosphere of LMDZ. We co-locate LMDZ outputs with IASI retrievals and we convolve these outputs by averaging kernels. We note the resulting time series $\delta^2H_{v\_LMDZ\_convol}$.

As expected, $\delta^2H_{v\_LMDZ\_convol}$ is smoothed compared to $\delta^2H_{v\_LMDZ}$, with the amplitude of variations in $\delta^2H_{v\_LMDZ\_convol}$ being 89 %, 95 % and 86 % with those in $\delta^2H_{v\_LMDZ}$ at the seasonal, intra-seasonal and synoptic scales (Table S4).

At all the time scales, the correlation coefficients between $\delta^2H_{v\_LMDZ\_convol}$ and $\delta^2H_{v\_IASI}$ are better than between $\delta^2H_{v\_LMDZ}$ and $\delta^2H_{v\_IASI}$ (Table S4). This is consistent with the fact that IASI observations are affected by instrument sensitivity compared to true profiles, and that we correctly account for this effect when calculating $\delta^2H_{v\_LMDZ\_convol}$.

1.2 Effect of random errors

IASI δ^2H measurements are affected by random errors (Lacour et al., 2012). The typical standard deviation for these errors is 40‰ in the TP. Therefore, at longer time scales, more samples are considered in the average, and thus the impact of random errors on average values is lower. Specifically, when averaging n samples, we expect the error on the average to be divided by $\sqrt{n}$. The fact that IASI is noisier and less correlated with LMDZ at short time scale may be an artifact of those random errors.

To estimate the impact of these errors on the observed variability, we use a Monte-Carlo approach in which we add random errors to LMDZ outputs. For each retrieved profile i, we draw a random number ε(i) from a Gaussian distribution with a null mean and a standard deviation of 40‰. We add this number to the δ^2H value that is simulated by LMDZ for this day t, $\widehat{\delta^2H_{LMDZ}}(t)$:

$$\delta^2H_{err}(i) = \widehat{\delta^2H_{LMDZ}}(t) + \varepsilon(i) \qquad (A1)$$

where the $\delta^2H_{err}(i)$ is the δ^2H value that is distorted by the random error. Throughout this appendix, the hat sign represents the daily average and the overbar sign represents the annual average.

We calculate a daily δ^2H time series $\widehat{\delta^2H_{err}}(t)$ by averaging all the δ^2H_{err} (i) values that belong to each given day. Finally, we estimate the correlation between the $\widehat{\delta^2H_{LMDZ}}(t)$ and $\widehat{\delta^2H_{err}}(t)$ time series. On average, 26.5 retrieved profiles in the Lijiang grid box are included in daily averages. This limits the effect of random errors. On average

over 10 Monte-Carlo simulations, the correlation coefficients between the $\delta^2\widehat{H_{LMDZ}}(t)$ and $\delta^2\widehat{H_{err}}(t)$ are 0.998, 0.974, 0.868 at the seasonal, intra and synoptic scales. Therefore, random errors may slightly distort $\delta^2H_{v\_IASI}$ time series at the synoptic scale, but not at longer time scales.

1.3 Effect of diurnal cycle

IASI observations with a global coverage are generally retrieved twice a day (orbits crossing the Equator at 9:30 and 21:30 LT). To estimate the impact of the diurnal cycle of water vapor isotopic composition, the time series of water vapor δ^2H are calculated based on morning and afternoon profiles separately. We decompose the daily-mean, grid-mean δ^2H, $\delta^2\widehat{H(t)}$ time series into :

$$\delta^2\widehat{H(t)} = P_m(t) \cdot \delta^2\widehat{H_m}(t) + (1 - P_m(t)) \cdot \delta^2\widehat{H_a}(t) \quad \text{(A2)}$$

where $\delta^2\widehat{H_m}(t)$ and $\delta^2\widehat{H_a}(t)$ are the daily-mean δ^2H retrieved in the morning and in the afternoon and $P_m(t)$ is the proportion of observations of water vapor in the morning on day t. We further decompose $P_m(t)$, $\delta^2\widehat{H_m}(t)$ and $\delta^2\widehat{H_a}(t)$ into the annual-mean $\overline{P_m}$, $\overline{\delta^2H_m}$ and $\overline{\delta^2H_a}$ plus their daily anomalies $P_m(t)'$, $\delta^2H_m(t)'$ and $\delta^2H_a(t)'$.

$$P_m(t) = \overline{P_m} + P_m(t)' \quad \text{(A3)}$$

$$\delta^2\widehat{H_m}(t) = \overline{\delta^2H_m} + \delta^2H_m(t)' \quad \text{(A4)}$$

$$\widehat{\delta^2H_a}(t) = \overline{\delta^2H_a} + \delta^2H_a(t)' \quad \text{(A5)}$$

We get the following decomposition:

$$\delta^2\widehat{H(t)} = \overline{P_m} \cdot \overline{\delta^2H_m} + (1 - \overline{P_m}) \cdot \overline{\delta^2H_a} + P_m(t)' \cdot \left(\overline{\delta^2H_m} - \overline{\delta^2H_a}\right) + \overline{P_m} \cdot \delta^2H_m(t)' + (1 - \overline{P_m}) \cdot \delta^2H_a(t)' + P_m(t)' \cdot (\delta^2H_m(t)' - \delta^2H_a(t)') \quad \text{(A6)}$$

The first and second terms on the right-hand sides stand for the annual-mean δ^2H in the morning and in the afternoon. The third term represents the effect of daily variations in the proportion of morning retrievals, named contrib_sampling. This represents the diurnal sampling bias. The fourth and fifth terms represent the effect of daily variations in the morning and in the afternoon δ^2H, named contrib_signal. This is the physical variability in which we are interested. The last term represents the effect of co-variability between the daily proportion anomalies and the δ^2H anomalies in the morning and in the afternoon, named contrib_cross.

δ^2H in the morning is correlated with δ^2H in the afternoon, but it is systematically more depleted than in the afternoon by -32.40‰ on average. The contribution of the sampling bias

to the daily-mean δ^2H variability is lower than 9% at all the time scales (Table S5, slopes of $\widehat{\delta^2 H}$ vs contrib_sampling). The daily mean δ^2H is very well correlated with contrib_signal at the seasonal and synoptic scales, but it is lower, though significant, at the intra-seasonal scale (Table S5). This means that the distortion of the daily-mean δ^2H variability by the diurnal sampling bias is slight.

1.4 Effect of inhomogeneous spatial sampling

In the daily δ^2H time series, every day represents an average of profiles that are located in a 3.6°x2.5° grid box. Inhomogeneous sampling in space can distort the daily-mean δ^2H time series if for some days, more profiles are located where the water vapor is more depleted or more enriched. At the scale of the grid box in such a mountainous region, we assume that the ground altitude z is the main controlling factor that leads to spatial variation of δ^2H within the grid box (Bowen et al., 2010). How variable are the altitudes at which the IASI profiles are located? What is the impact of this variability on the daily δ^2H time series? This is what we aim at quantifying here.

We thus decompose the altitude range into nz small intervals, each representing altitudes z to z+dz (nz = 40, dz = 0.2 km, first interval starting at altitude z = 0 km). For each day t, the daily-mean, grid-mean $\delta^2 H$, $\widehat{\delta^2 H(t)}$ is given by:

$$\widehat{\delta^2 H(t)} = \sum_{z=1}^{nz} p(t,z) \cdot \delta^2 H(t,z) \qquad \text{(A7)}$$

where p(t, z) is the probability density function for a given day t and altitude interval z and δ^2H (t, z) is the daily mean δ^2H for a given day t and altitude interval z.

We further decompose p(t, z) and δ^2H (t, z) into their annual averages and their anomalies :

$$p(t,z) = \overline{p(z)} + p(t,z)' \qquad \text{(A8)}$$

$$\delta^2 H(t,z) = \overline{\delta^2 H(z)} + \delta^2 H(t,z)' \qquad \text{(A9)}$$

where $\overline{\delta^2 H(z)}$ and $\overline{p(z)}$ represent the annual-mean $\delta^2 H$ and probability density functions when binned as function of z.

$$\overline{\delta^2 H(z)} = \frac{\sum_{t=1}^{nt} p(t,z) \cdot \delta^2 H(t,z)}{\sum_{t=1}^{nt} p(t,z)} \qquad \text{(A10)}$$

$$\overline{p(z)} = \sum_{t=1}^{nt} p(t,z) \qquad \text{(A11)}$$

and $p(t,z)'$ and $\delta^2 H(t,z)'$ represent the daily anomalies of p(t,z) and $\delta^2 H$ (t, z):

$$\delta^2 H(t,z)' = \delta^2 H(t,z) - \overline{\delta^2 H(z)} \qquad \text{(A12)}$$

$$p(t,z)' = \frac{p(t,z)}{\sum_{z=1}^{nz} p(t,z)} - \overline{p(z)} \qquad \text{(A13)}$$

We get the following decomposition:

$$\widehat{\delta^2 H(t)} = \sum_{z=1}^{nz} \overline{p(z)} \cdot \overline{\delta^2 H(z)} + \sum_{z=1}^{nz} \overline{p(z)} \cdot \delta^2 H(t,z)' +$$

$$\sum_{z=1}^{nz} p(t,z)' \cdot \overline{\delta^2 H(z)} + \sum_{z=1}^{nz} p(t,z)' \cdot \delta^2 H(t,z)' \qquad \text{(A14)}$$

The first term on the right-hand side is constant and corresponds to the annual-mean δ^2H. The second term is the effect of temporal variations in δ^2H at different altitudes, named contrib_signal. This is the variability unbiased by sampling inhomogeneities. The third term is the effect of temporal variations in the altitude probability density function, named contrib_sampling. It represents the effect of inhomogeneous spatial sampling. The fourth term represents the effect of co-variability between vertical profiles of probability density function and δ^2H, named contrib_cross.

The contribution of contrib_sampling to the daily-mean δ^2H variability is lower than 2% (Table S6, slopes of $\widehat{\delta^2 H}$ vs contrib_sampling). $\widehat{\delta^2 H}$ is well correlated with contrib_signal with the correlation coefficients from 0.99 at the seasonal scale to 0.88 at the synoptic scale (Table S6). This means that the effect of sampling heterogeneities is small. The $\widehat{\delta^2 H}$ is well correlated with contrib_cross at all time scales. The contrib_cross term contributes from 17% at seasonal scale to 34% at synoptic time scale. This may contribute to the relatively lower correlation between δ^2H simulated by LMDZ and observed by IASI at shorter time scales compared to the seasonal scale (Table 5).

1.5 Synthesis: effect of IASI errors on the decomposition of daily $\boldsymbol{\delta^2}$H

In section 2.2.2, we introduce a decomposition method to better interpret the daily δ^2H_p variability. How do the errors examined above affect the results of this decomposition? With this aim, we calculate the daily water vapor δ^2H that IASI would observe if it was flying over the atmosphere of LMDZ. First, we co-locate the simulated δ^2H_v with IASI retrievals and we convolve these outputs by averaging kernels, to account for instrument sensitivity (Appendix 1.1); Second, random errors are added to the convolved δ^2H_v time series (Appendix 1.2); Third, the contrib_sampling time series calculated in Appendix 1.3 (diurnal sampling) and the contrib_sampling time series calculated in Appendix 1.4 (spatial sampling) are added to the convolved and randomly-distorted δ^2H_v time series. We get $\delta^2H_{v\_lmdz\_errors}$.

Table 6 and Table S6 show the correlation coefficients and slopes of the three different contributions as a function of the δ^2H_p simulated by LMDZ. It is the same as Table 2 but for LMDZ instead of IASI. Table 6 uses δ^2H_v simulated directly by LMDZ, whereas Table S7 uses $\delta^2H_{v\_lmdz\_errors}$, i.e. after accounting for errors as in IASI.

At the seasonal scale, IASI errors tend to strengthen the contribution of large-scale processes, and to reduce the contribution of local processes (and even make them look negative). Therefore, the fact that in IASI the contribution of local processes dominates (Table

2) is probably very robust, and without errors the importance of local processes would probably be even greater.

At the intra-seasonal and synoptic scales, IASI errors tend to decrease the correlations between δ^2H_p and its contributions. Errors slightly reduce the contribution of local processes at the intra-seasonal scale and enhance them at the synoptic scale, but without dramatically modifying the results. We can thus expect the decomposition in Table 4 to be robust with respect to IASI errors at these time scales, results would be probably qualitatively similar without IASI errors.

Acknowledgments

This research was supported by the National Natural Science Foundation of China (91647101 and 41401083), the strategic priority research program of the Chinese Academy of Sciences (No: XDA19070503) and the State Key Laboratory of Cryospheric Sciences (SKLCS-ZZ-2020, SKLCS-OP-2019-10). This work was granted access to the HPC resources of IDRIS under the allocation 0292 made by GENCI. We thank all SWING2 members for producing and making available their model outputs. SWING2 was supported by the Isotopic Hydrology Programme at the International Atomic Energy Agency. This study was funded by China Scholarship Council under the file number 201806180069. The in-situ isotopic and meteorological observations used in this study, together with the LMDZ outputs and the IASI observations, have been published on the Pangea data repository https://doi.pangaea.de/10.1594/PANGAEA.910848.

References

Battisti, D. S., Ding, Q., & Roe, G. H. (2014). Coherent pan-Asian climatic and isotopic response to orbital forcing of tropical insolation. *Journal of Geophysical Research: Atmospheres*, *119*(21), 11-997.

Bony, S., Risi, C., & Vimeux, F. (2008). Influence of convective processes on the isotopic composition ($\delta^{18}O$ and δD) of precipitation and water vapor in the tropics: 1. Radiative-convective equilibrium and Tropical Ocean–Global Atmosphere–Coupled Ocean-Atmosphere Response Experiment (TOGA-COARE) simulations. *Journal of Geophysical Research: Atmospheres*, *113* (D19).

Botsyun, S., Sepulchre P., Risi C. & Donnadieu, Y. (2016). Impacts of Tibetan Plateau uplift on atmospheric dynamics and associated precipitation $\delta^{18}O$. *Climate of the Past*, 12, 1401-1420.

Botsyun, S., Sepulchre, P., Donnadieu, Y., Risi, C., Licht, A., & Rugenstein, J. K. C. (2019). Revised paleoaltimetry data show low Tibetan Plateau elevation during the Eocene. *Science*, *363*(6430), 1436.

Bowen, G. J. (2010). Isoscapes: spatial pattern in isotopic biogeochemistry. *Annual review of earth and planetary sciences*, *38*, 161-187.

Cai, Z., Tian, L. (2016). Atmospheric controls on seasonal and interannual variations in the precipitation isotope in the East Asian Monsoon region. *Journal of Climate*, 29, 1339-1352.

Cai, Z., Tian, L., Bowen, G.J. (2017). ENSO variability reflected in precipitation oxygen isotopes across the Asian Summer Monsoon region. *Earth and Planetary Science Letters*, 475, 25-33.

Cai, Z., Tian, L., & Bowen, G. J. (2018). Spatial-seasonal patterns reveal large-scale atmospheric controls on Asian Monsoon precipitation water isotope ratios. *Earth and Planetary Science Letters*, 503, 158-169.

Cai, Z., Tian, L., & Bowen, G. J. (2019). Influence of recent climate shifts on the relationship between ENSO and Asian Monsoon precipitation oxygen isotope ratios. *Journal of Geophysical Research: Atmospheres*, 124, 7825-7835.

Cui, B. L., & Li, X. Y. (2015). Stable isotopes reveal sources of precipitation in the Qinghai Lake Basin of the northeastern Tibetan Plateau. *Science of the Total Environment*, *527*, 26-37.

Che, Y., Zhang, M., Wang, S., Wang, J., Liu, Y. & Zhang, F. (2016). Stable water isotopes of precipitation in China simulated by SWING2 models. *Arabian Journal of Geosciences*, 9(19), 732.

Dansgaard, W. (1964) Stable isotopes in precipitation. *Tellus 16*, 436-468.

Dee, D. P., Uppala, S. M., Simmons, A. J., Berrisford, P., Poli, P., Kobayashi, S., Andrae, U., et al. (2011) The ERA-Interim reanalysis: configuration and performance of the data assimilation system. *Quarterly Journal of the royal meteorological society*, *137*(656), 553-597.

Dong, W., Lin, Y., Wright, J. S., Ming, Y., Xie, Y., Wang, B., Luo, Y., et al. (2016). Summer rainfall over the southwestern Tibetan Plateau controlled by deep convection over the Indian subcontinent. *Nature communications*, *7*, 10925.

Dufresne, J. L., Foujols, M. A., Denvil, S., Caubel, A., Marti, O., Aumont, O., Balkanski, Y., et al. (2013) Climate change projections using the IPSL-CM5 Earth System Model: from CMIP3 to CMIP5. *Climate Dynamics*, *40*, 2123-2165.

Dütsch, M., Pfahl, S., & Wernli, H. (2016). Drivers of δ^2H variations in an idealized extratropical cyclone. *Geophysical Research Letters*, *43*(10), 5401-5408.

Dütsch, M., Pfahl, S., Meyer, M., & Wernli, H. (2018). Lagrangian process attribution of isotopic variations in near-surface water vapour in a 30-year regional climate simulation over Europe. *Atmospheric Chemistry and Physics*, *18*(3), 1653-1669.

Ehlers, T. A., & Poulsen, C. J. (2009). Influence of Andean uplift on climate and paleoaltimetry estimates. *Earth and Planetary Science Letters*, *281*(3-4), 238-248.

Field, R. D., Jones, D. B., & Brown, D. P. (2010). Effects of postcondensation exchange on the isotopic composition of water in the atmosphere. *Journal of Geophysical Research: Atmospheres*, *115*(D24).

Frankenberg, C., Yoshimura, K., Warneke, T., Aben, I., Butz, A., Deutscher, N., Griffith, D., et al. (2009). Dynamic processes governing lower-tropospheric HDO/H2O ratios as observed from space and ground. *Science*, *325*(5946), 1374-1377.

Frankenberg, C., Wunch, D., Toon, G., Risi, C., Scheepmaker, R., Lee, J. E., Wennberg, P., et al. (2013). Water vapor isotopologue retrievals from high-resolution GOSAT shortwave infrared spectra. *Atmospheric Measureme Techniques*, *6*(2), 263-274.

Gao, J., Masson-Delmotte, V., Yao, T., Tian, L., Risi, C., & Hoffmann, G. (2011). Precipitation water stable isotopes in the south Tibetan Plateau: observations and modeling. *Journal of Climate*, *24*(13), 3161-3178.

Gao, J., Masson-Delmotte, V., Risi, C., He, Y., & Yao, T. (2013). What controls precipitation δ18O in the southern Tibetan Plateau at seasonal and intra-seasonal scales? A case study at Lhasa and Nyalam. *Tellus B: Chemical and Physical Meteorology*, *65*(1), 21043.

Galewsky, J., & Hurley, J. V. (2010). An advection-condensation model for subtropical water vapor isotopic ratios. *Journal of Geophysical Research: Atmospheres*, *115*(D16).

Galewsky, J., Steen-Larsen, H. C., Field, R. D., Worden, J., Risi, C., & Schneider, M. (2016). Stable isotopes in atmospheric water vapor and applications to the hydrologic cycle. *Reviews of Geophysics*, *54*(4), 809-865.

Gao, J., He, Y., Masson-Delmotte, V., & Yao, T. (2018). ENSO effects on annual variations of summer precipitation stable isotopes in Lhasa, southern Tibetan Plateau. *Journal of Climate*, *31*(3), 1173-1182.

Graf, P., Wernli, H., Pfahl, S., & Sodemann, H. (2019). A new interpretative framework for below-cloud effects on stable water isotopes in vapour and rain. *Atmospheric Chemistry and Physics*, *19*(2), 747-765.

Guo, X., Tian, L., Wen, R., Yu, W., & Qu, D. (2017). Controls of precipitation δ18O on the northwestern Tibetan Plateau: A case study at Ngari station. *Atmospheric research*, *189*, 141-151.

He, Y., Risi, C., Gao, J., Masson-Delmotte, V., Yao, T., Lai, C.-T., et al. (2015). Impact of atmospheric convection on south Tibet summer precipitation isotopologue composition using a combination of in situ measurements, satellite data, and atmospheric general circulation modeling. *Journal of Geophysical Research: Atmospheres*, *120*(9), 3852-3871.

He, S., & Richards, K. (2016). Stable isotopes in monsoon precipitation and water vapour in Nagqu, Tibet, and their implications for monsoon moisture. *Journal of Hydrology*, *540*, 615-622.

Hourdin, F., Musat, I., Bony, S., Braconnot, P., Codron, F., Dufresne, J. L., Fairhead, L., et al. (2006). The LMDZ4 general circulation model: climate performance and sensitivity to parametrized physics with emphasis on tropical convection. *Climate Dynamics*, *27*(7-8), 787-813.

Huffman, G. J., Bolvin, D. T., Nelkin, E. J., Wolff, D. B., Adler, R. F., Gu, G., Hong, Y., et al. (2007). The TRMM multisatellite precipitation analysis (TMPA): Quasi-global, multiyear, combined-sensor precipitation estimates at fine scales. *Journal of hydrometeorology*, *8*(1), 38-55.

Hu, J., Emile-Geay, J., Tabor, C., Nusbaumer, J., & Partin, J. (2019). Deciphering oxygen isotope records from Chinese speleothems with an isotope-enabled climate model. *Paleoceanography and Paleoclimatology*. https://doi.org/10.1029/2019PA003741.

Ishizaki, Y., Yoshimura, K., Kanae, S., Kimoto, M., Kurita, N., & Oki, T. (2012). Interannual variability of $H_2{}^{18}O$ in precipitation over the Asian monsoon region. *Journal of Geophysical Research: Atmospheres,*117, 16308.

Kalnay, E., Kanamitsu, M., Kistler, R., Collins, W., Deaven, D., Gandin, L., Iredell, M., et al. (1996). The NCEP/NCAR 40-year reanalysis project. *Bulletin of the American meteorological Society*, *77*(3), 437-472.

Kaspari, S., Mayewski, P., Kang, S., Sneed, S., Hou, S., Hooke, R., Kreutz, K., et al. (2007). Reduction in northward incursions of the South Asian monsoon since∼ 1400 AD inferred from a Mt. Everest ice core. *Geophysical Research Letters*, *34*(16).Kong, Y., Wang, K., Pu, T., & Shi, X. (2019a). Non-monsoon precipitation dominates groundwater recharge beneath a monsoon affected glacier in Tibetan Plateau. *Journal of Geophysical Research: Atmospheres.* https://doi.org/10.1029/2019JD030492.

Kong, Y., Wang, K., Li, J., & Pang, Z. (2019b). Stable Isotopes of Precipitation in China: A Consideration of Moisture Sources. *Water, 11(6),* 1239.

Krishnamurthy, V., Goswami, B.N. (2000). Indian monsoon-ENSO relationship on interdecadal timescale. *Journal of Climate,* 13, 579–595.

Kurita, N. (2013). Water isotopic variability in response to mesoscale convective system over the tropical ocean. *Journal of Geophysical Research: Atmospheres*, *118*(18), 10-376.

Lacour, J. L., Risi, C., Clarisse, L., Bony, S., Hurtmans, D., Clerbaux, C., & Coheur, P. F. (2012). Mid-tropospheric δD observations from IASI/MetOp at high spatial and temporal resolution. *Atmospheric chemistry and physics*, *12*(22), 10817-10832.

Lacour, J.-L., Clarisse, L., Worden, J., Schneider, M., Barthlott, S., Hase, F., Risi, C., et al. (2015). Cross-validation of IASI/MetOp derived tropospheric δD with TES and ground-based FTIR observations. DOI : 10.5194/amt-8-1447-2015

Lacour, J. L., Risi, C., Worden, J., Clerbaux, C., & Coheur, P. F. (2018). Importance of depth and intensity of convection on the isotopic composition of water vapor as seen from IASI and TES δD observations. *Earth and planetary science letters*, *481*, 387-394.

Lawrence, J. R., Gedzelman, S. D., Dexheimer, D., Cho, H. K., Carrie, G. D., Gasparini, R., Anderson, C. R., et al. (2004). Stable isotopic composition of water vapor in the tropics. *Journal of Geophysical Research: Atmospheres*, *109*(D6).

Lee, J.E., Risi, C., Fung, I., Worden, J., Scheepmaker, R.A., Lintner, B., & Frankenberg, C. (2012). Asian monsoon hydrometeorology from TES and SCIAMACHY water vapor isotope measurements and LMDZ simulations: Implications for speleothem climate record interpretation. Journal of Geophysical Research: Atmospheres, 117(D15).

Liu, X., Shen, J., Wang, S., Wang, Y., & Liu, W. (2007). Southwest monsoon changes indicated by oxygen isotope of ostracode shells from sediments in Qinghai Lake since the late Glacial. *Chinese Science Bulletin,* 52(4), 539.Majoube, M. (1971). Fractionation of

oxygen 18 and deuterium between water and its vapor. *Journal of Physical Chemistry , 68* , 1423-1436.

Moore, M., Kuang, Z., & Blossey, P. N. (2014). A moisture budget perspective of the amount effect. *Geophysical Research Letters*, *41*(4), 1329-1335.

Moore, M., Blossey, P. N., Muhlbauer, A., & Kuang, Z. (2016). Microphysical controls on the isotopic composition of wintertime orographic precipitation. *Journal of Geophysical Research: Atmospheres*, *121*(12), 7235-7253.

Morrill, C., Overpeck, J. T., Cole, J. E., Liu, K. B., Shen, C., & Tang, L. (2006). Holocene variations in the Asian monsoon inferred from the geochemistry of lake sediments in central Tibet. *Quaternary Research*, *65*(02), 232-243.

Pang, H., He, Y., Lu, A., Zhao, J., Ning, B., Yuan, L., & Song, B. (2006). Synoptic-scale variation of δ 18 O in summer monsoon rainfall at Lijiang, China. *Chinese Science Bulletin*, *51*(23), 2897-2904.

Pausata, F.S., Battisti, D.S., Nisancioglu, K.H., & Bitz, C.M. (2011). Chinese stalagmite $\delta^{18}O$ controlled by changes in the Indian monsoon during a simulated Heinrich event. Nature Geoscience, 4(7), 474.

Poulsen, C. J., & Jeffery, M. L. (2011). Climate change imprinting on stable isotopic compositions of high-elevation meteoric water cloaks past surface elevations of major orogens. *Geology*, *39*(6), 595-598.

Pu, T., Qin, D. H. Kang, S. C., Niu, H. W., He, Y. Q. & Wang, S. J. (2017) Water isotopes and hydrograph separation in different glacial catchments in the southeast margin of the Tibetan Plateau. *Hydrological Processes. 31*, 3810-3826.

Ramírez, I. J., & Briones, F. (2017). Understanding the El Niño costero of 2017: The definition problem and challenges of climate forecasting and disaster responses. *International Journal of Disaster Risk Science*, *8*(4), 489-492.

Ren, W., Yao, T., & Xie, S. (2017). Key drivers controlling the stable isotopes in precipitation on the leeward side of the central Himalayas. *Atmospheric research, 189*, 134-140.Risi, C., Bony, S., Vimeux, F., Descroix, L., Ibrahim, B., Lebreton, E., Mamadou, I. & Sultan, B. (2008a). What controls the isotopic composition of the African monsoon precipitation? Insights from event-based precipitation collected during the 2006 AMMA field campaign. *Geophysical Research Letters*, *35*(24).

Risi, C., Bony, S., & Vimeux, F. (2008b). Influence of convective processes on the isotopic composition (δ18O and δD) of precipitation and water vapor in the tropics: 2. Physical interpretation of the amount effect. *Journal of Geophysical Research: Atmospheres*, *113*(D19).

Risi, C., Bony, S., Vimeux, F., & Jouzel, J. (2010a). Water-stable isotopes in the LMDZ4 general circulation model: Model evaluation for present-day and past climates and applications to climatic interpretations of tropical isotopic records. *Journal of Geophysical Research: Atmospheres*, *115*(D12).

Risi, C., Bony, S., Vimeux, F., Chong, M., & Descroix, L. (2010b). Evolution of the stable water isotopic composition of the rain sampled along Sahelian squall lines. *Quarterly Journal of the Royal Meteorological Society*, *136*(S1), 227-242.

Risi, C., Bony, S., Vimeux, F., Frankenberg, C., Noone, D., & Worden, J. (2010c). Understanding the Sahelian water budget through the isotopic composition of water vapor and precipitation. *Journal of Geophysical Research: Atmospheres*, *115*(D24).

Risi, C., Noone, D., Worden, J., Frankenberg, C., Stiller, G., Kiefer, M., Funke, B., et al. (2012) Process-evaluation of tropospheric humidity simulated by general circulation models using water vapor isotopologues: 1. Comparison between models and observations. *Journal of Geophysical Research: Atmospheres*, *117*(D5).

Risi, C., Noone, D., Frankenberg, C., & Worden, J. (2013). Role of continental recycling in intraseasonal variations of continental moisture as deduced from model simulations and water vapor isotopic measurements. *Water Resources Research*, *49*(7), 4136-4156.

Rowley, D. B., & Currie, B. S. (2006). Palaeo-altimetry of the late Eocene to Miocene Lunpola basin, central Tibet. *Nature*, *439*(7077), 677.

Rowley, D. B. (2007a). Stable isotope-based paleoaltimetry: Theory and validation. *Reviews in Mineralogy and Geochemistry*, *66*(1), 23-52.

Rowley, D. B. & Garzione, C. N. (2007b). Stable Isotope-Based Paleoaltimetry. *Annual Review of Earth and Planetary Sciences*, 35, 463-508.

Shao, L., Tian, L., Cai, Z., Cui, J., Zhu, D., Chen, Y., & Palcsu, L. (2017). Driver of the interannual variations of isotope in ice core from the middle of Tibetan Plateau. *Atmospheric research*, *188*, 48-54.

Shen, H., & Poulsen, C. J. (2019). Precipitation $\delta^{18}O$ on the Himalaya–Tibet orogeny and its relationship to surface elevation. *Climate of the Past*, *15*(1), 169-187.

Shi, X., Pu, T., He, Y., Qi, C., Zhang, G., & Xia, D. (2017). Variability of Stable Isotope in Lake Water and Its Hydrological Processes Identification in Mt. Yulong Region. *Water*, *9*(9), 711.

Tan, M. (2014). Circulation effect: response of precipitation $\delta^{18}O$ to the ENSO cycle in monsoon regions of China. *Climate Dynamics*, 42, 1067-1077.

Tabor, C.R., Otto-Bliesner, B.L., Brady, E.C., Nusbaumer, J., Zhu, J., Erb, M.P., Wong, T.E., et al. (2018). Interpreting Precession-Driven $\delta^{18}O$ Variability in the South Asian Monsoon Region. *Journal of Geophysical Research: Atmospheres*, *123*(11), 5927-5946.millen

Thompson, L. G., Mosley-Thompson, E., Davis, M. E., Bolzan, J. F., Dai J., Klein, L., Gundestrup, N., Yao, T., Wu, x. & Xie, Z. (1990). Glacial stage ice-core records from the subtropical Dunde ice cap, China. *Annals of Glaciology*, *14*, 288-297.

Thompson, L. G., Yao, T., Mosley-Thompson, E., Davis, M. E., Henderson, K. A., & Lin, P. N. (2000). A high-resolution millennial record of the South Asian monsoon from Himalayan ice cores. *Science*, *289*(5486), 1916-1919.

Thompson, L. G., Mosley-Thompson, E., & Henderson, K. A. (2000b). Ice-core palaeoclimate records in tropical South America since the Last Glacial Maximum. *Journal of Quaternary Science: Published for the Quaternary Research Association*, *15*(4), 377-394.

Tian, L., Yao, T., Numaguti, A., & Sun, W. (2001a). Stable isotope variations in monsoon precipitation on the Tibetan Plateau. *Journal of the Meteorological Society of Japan. Ser. II*, *79*(5), 959-966.

Tian, L., Masson-Delmotte, V., Stievenard, M., Yao, T., & Jouzel, J. (2001b). Tibetan Plateau summer monsoon northward extent revealed by measurements of water stable isotopes. *Journal of Geophysical Research: Atmospheres*, *106*(D22), 28081-28088.

Tian, L., Yao, T., Sun, W., Stievenard, M., & Jouzel, J. (2001c). Relationship between δD and $\delta^{18}O$ in precipitation on north and south of the Tibetan Plateau and moisture recycling. *Science in China Series D: Earth Sciences*, *44*(9), 789-796.

Tian, L., Yao, T., Schuster, P. F., White, J. W. C., Ichiyanagi, K., Pendall, E., Pu, J. Et al. (2003). Oxygen-18 concentrations in recent precipitation and ice cores on the Tibetan Plateau. *Journal of Geophysical Research: Atmospheres*, *108*(D9).

Tian, L., Yao, T., White, J. W. C., Yu. W, & Wang, N. (2005). Westerly moisture transport to the middle of Himalayas revealed from the high deuterium excess. *Chinese Science Bulletin*, *50*(10), 1026-1030.

Tian, L., Yao, T., MacClune, K., White, J.W.C., Schilla, A., Vaughn, B., Vachon, R., et al. (2007). Stable isotopic variations in west China: A consideration of moisture sources. *Journal of Geophysical Research: Atmospheres*, *112*(D10).

Tian, L., Ma, L., Yu, W., Liu, Z., Yin, C., Zhao, Z., Tang, W. & Wang, Y. (2008). Seasonal variations of stable isotope in precipitation and moisture transport at Yushu, eastern Tibetan Plateau. *Science in China Series D: Earth Sciences*, *51*(8), 1121-1128.

Tremoy, G., Vimeux, F., Mayaki, S., Souley, I., Cattani, O., Risi, C., Favreau, G., et al. (2012). A 1-year longδ18O record of water vapor in Niamey (Niger) reveals insightful atmospheric processes at different timescales. *Geophysical Research Letters*, *39*(8).

Uppala, S. M., Kållberg, P. W., Simmons, A. J., Andrae, U., Bechtold, V. D. C., Fiorino, M., Gibson, K., et al. (2005) The ERA-40 re-analysis. *Quarterly Journal of the Royal Meteorological Society: A journal of the atmospheric sciences, applied meteorology and physical oceanography*, *131*(612), 2961-3012.

Vimeux, F., Gallaire, R., Bony, S., Hoffmann, G., & Chiang, J. C. (2005). What are the climate controls on δD in precipitation in the Zongo Valley (Bolivia)? Implications for the Illimani ice core interpretation. *Earth and Planetary Science Letters*, *240*(2), 205-220.

Vimeux, F., Tremoy, G., Risi, C., & Gallaire, R. (2011). A strong control of the South American SeeSaw on the intra-seasonal variability of the isotopic composition of precipitation in the Bolivian Andes. *Earth and Planetary Science Letters*, *307*(1-2), 47-58.

Wang, B. (2006). The Asian monsoon. New York: Springer-Verlag Berlin Heidelberg. https://doi.org/10.1007/3-540-37722-0.

Wang, B., Ding, Q., & Joseph, P. V. (2009). Objective definition of the Indian summer monsoon onset. *Journal of Climate*, *22*(12), 3303-3316.

Wang, W., Wu, T. H., Zhao, L., Li, R., Zhu, X. F., Wang, W. R., Yang, S. H., Qin, Y. H. & Hao, J. M. (2018). Exploring the ground ice recharge near permafrost table on the central Qinghai-Tibet Plateau using chemical and isotopic data. *Journal of Hydrology*, *560*, 220-229.

Wang, D., Tian, L., Cai, Z., Shao, L., Guo, X., Tian, R., Li, Y., et al. (2020). Indian monsoon precipitation isotopes linked with high level cloud cover at local and regional scales. *Earth and Planetary Science Letters*, *529*,115837.

Worden, J., Bowman, K., Noone, D., Beer, R., Clough, S., Eldering, A., Fisher, B., et al. (2006). Tropospheric Emission Spectrometer observations of the tropospheric HDO/H2O ratio: Estimation approach and characterization. *Journal of Geophysical Research: Atmospheres*, *111*(D16).

Worden, J., Noone, D., Bowman, K., Beer, R., Eldering, A., Fisher, B., Gunson, M., et al. (2007). Importance of rain evaporation and continental convection in the tropical water cycle. *Nature*, *445*(7127), 528.

Worden, J., Kulawik, S., Frankenberg, C., Payne, V., Bowman, K., Cady-Pereira, K., Wecht, K., et al. (2012). Profiles of CH_4, HDO, H_2O, and N_2O with improved lower tropospheric vertical resolution from Aura TES radiances. *Atmospheric Measurement Techniques Discussions*, *4*(6), 6679-6721.

Xie, S.-P., Du, Y., Huang, G., Zheng, X.-T., Tokinaga, H., Hu, K., & Liu, Q. (2010). Decadal shift in El Niño influences on Indo–Western Pacific and East Asian climate in the 1970s. *Journal of Climate*, 23(12), 3352–3368.

Yang, B., Braeuning, A., Yao, T., Davis, M.E. (2007). Correlation between the oxygen isotope record from Dasuopu ice core and the Asian Southwest Monsoon during the last millennium. *Quaternary Science Reviews*, 26(13-14), 1810-1817.

Yao, T., Thompson, L. G., Mosley-Thompson, E., Zhihong, Y., Xingping, Z., & Lin, P. N. (1996). Climatological significance of δ18O in north Tibetan ice cores. *Journal of Geophysical Research: Atmospheres*, *101*(D23), 29531-29537.

Yao, T., Shi, Y., & Thompson, L. G. (1997a). High resolution record of paleoclimate since the Little Ice Age from the Tibetan ice cores. *Quaternary International*, *37*, 19-23.

Yao, T., Thompson, L. G., Shi, Y., Qin, D., Jiao, K., Yang, Z., Tian, L., et al. (1997b). Climate variation since the last interglaciation recorded in the Guliya ice core. *Science in China Series D: Earth Sciences*, *40*(6), 662-668.

Yao, T., Thompson, L., Yang, W., Yu, W., Gao, Y., Guo, X., Yang, X., et al. (2012). Different glacier status with atmospheric circulations in Tibetan Plateau and surroundings. *Nature climate change*, *2*(9), 663-667.

Yao, T., Masson-Delmotte, V., Gao, J., Yu, W., Yang, X., Risi, C., Sturm, C., et al. (2013). A review of climatic controls on $\delta^{18}O$ in precipitation over the Tibetan Plateau: Observations and simulations. *Reviews of Geophysics*, *51*(4), 525-548.

Yu, W., Yao, T., Tian, L., Wang, Y., Li, Z. & Sun, W. (2006). Oxygen-18 isotopes in precipitation on the eastern Tibetan Plateau. *Annals of Glaciology*, *43*, 263-268.

Yu, W., Yao, T., Tian, L., Ma, Y., Kurita, N., Ichiyanagi, K., Wang, Y. & Sun, W. (2007). Stable isotope variations in precipitation and moisture trajectories on the western Tibetan Plateau, China. *Arctic, Antarctic, and Alpine Research*, *39*(4), 688-693.

Yu, W., Yao, T., Tian, L., Ma, Y., Ichiyanagi, K., Wang, Y., & Sun, W. (2008). Relationships between $\delta^{18}O$ in precipitation and air temperature and moisture origin on a south-north transect of the Tibetan Plateau. *Atmospheric Research*, *87*(2), 158-169.

Yu, W., Yao, T., Lewis, S., Tian, L., Ma, Y., Xu, B., & Qu, D. (2014). Stable oxygen isotope differences between the areas to the north and south of Qinling Mountains in China reveal different moisture sources. *International Journal of Climatology*, *34*(6), 1760-1772.

Yu, W., Wei, F., Ma, Y., Liu, W., Zhang, Y., Luo, L., Tian, L., et al. (2016a). Stable isotope variations in precipitation over Deqin on the southeastern margin of the Tibetan Plateau during different seasons related to various meteorological factors and moisture sources. *Atmospheric research*, *170*, 123-130.

Yu, W., Yao, T., Tian, L., Ma, Y., Wen, R., Devkota, L. P., Wang, W., et al. (2016b). Short-term variability in the dates of the Indian monsoon onset and retreat on the southern and northern slopes of the central Himalayas as determined by precipitation stable isotopes. *Climate dynamics*, *47*(1-2), 159-172.

Yu, W., Tian, L., Risi, C., Yao, T., Ma, Y., Zhao, H., Zhu, H.,et al. (2016c). $\delta^{18}O$ records in water vapor and an ice core from the eastern Pamir Plateau: Implications for paleoclimate reconstructions. *Earth and Planetary Science Letters*, *456*, 146-156.

Zhang, X., Nakawo, M., Yao, T., Han, J., & Xie, Z. (2002). Variations of stable isotopic compositions in precipitation on the Tibetan Plateau and its adjacent regions. *Science in China Series D: Earth Sciences*, 45(6), 481-493.

Table 1 Correlation coefficients between δ^2H_p and local temperature (T), precipitation (P), relative humidity (RH), Indian summer index (ISM), wind direction (WD) and trajectory direction (TD) at different time scales (raw, seasonal, intra-seasonal and synoptic scale)

Time scale		δ^2H vs P	δ^2H vs T	δ^2H vs RH	δ^2H vs WD	δ^2H vs TD	δ^2H vs ISM
Raw data	Slope	-	-3.92	-1.51	0.02	-	-2.5
	r	-0.22	-0.28*	-0.32**	0.18	0.15	-0.38**
Seasonal time scale	Slope	-4.57	-8.74	-5.41	0.03	0.005	-3.85
	r	-0.26*	-0.75**	-0.80**	0.94**	0.70**	-0.75**
Intra-seasonal time scale	Slope	-	-4.66	-	0.03	0.01	-5.18
	r	-0.09	-0.24*	0.15	0.60**	0.53**	-0.41**
Synoptic time scale	Slope	-0.64	4.29	-0.92	-	-	-
	r	-0.27*	0.33**	-0.24*	-0.02	-0.04	0.13

Notes: *, ** indicates that the correlations are significant within a 0.05 or 0.01 confidence limit. Only the slopes with significant correlations at the 0.05 and 0.01 level are shown.

Table 2 Correlation coefficients and slopes of the 3 different contributions based on the δ^2H_{vLS} observed by IASI as a function of δ^2H_p observed at Lijiang at different time scales. Correlations between some contributions and relative humidity (RH) and wind direction (WD) are also given.

Time scale		$\alpha' \cdot R_{veq}$	$\overline{\alpha} \cdot R_{vLS}$	$\overline{\alpha} \cdot (R_{veq}-R_{vLS})$	RH vs $\overline{\alpha} \cdot (R_{veq} - R_{vLS})$	WD vs $\overline{\alpha} \cdot R_{vLS}$	WD vs $\overline{\alpha} \cdot (R_{veq}-R_{vLS})$
Raw data	Slope	-	-	0.82	-	-	-
	r	-0.21	0.17	0.65**	-0.34	-0.09	0.18
Seasonal time scale	Slope	-0.007	0.27	0.69	-5.82	6.61	22.15
	r	-0.92**	0.81**	0.97**	-0.91**	0.62**	0.97**
Intra-seasonal time scale	Slope	-0.007	-0.21	1.15	-1.87	-10.15	20.42
	r	-0.49**	-0.32**	0.90**	-0.33**	-0.76**	0.79**
Synoptic time scale	Slope	-	-	0.68	-	-	-
	r	0.20	0.24	0.46**	-0.20	-0.04	0.02

Notes: *, ** indicates that the correlations are significant within a 0.05 or 0.01 confidence limit.

Table 3 Correlation coefficient between δ^2H in precipitation at Lijiang and in Mount Meili region (MY, TZ, LH)

Seasonal time scale	Lijiang	MY	TZ	LH
Lijiang	1	0.91** (23)	0.94** (23)	0.88** (30)
MY		1	0.97** (34)	0.97** (34)
TZ			1	0.98** (46)
LH				1

Intra-seasonal time scale	Lijiang	MY	TZ	LH
Lijiang	1	-0.04 (23)	0.44* (23)	0.36 (30)
MY		1	0.77** (34)	0.93** (34)
TZ			1	0.71** (46)
LH				1

Synoptic time scale	Lijiang site	MY	TZ	LH
Lijiang	1	0.05 (23)	-0.009 (23)	0.29 (30)
MY		1	0.73** (34)	0.64** (34)
TZ			1	0.71** (46)
LH				1

Notes: *, ** indicates that the correlations are significant within a 0.05 or 0.01 confidence limit. Number in the parentheses represents the number of precipitation samples in 2017-2018. MY, TZ, LH represent the Mingyong, Taizimiao and Lianhuasi, respectively, which is distributed in the Mt. Meili region.

Table 4 First column: Correlation coefficients and slopes of the δ^2H_p simulated by SWING2 ($\delta^2H_{p\_SWING2}$) models as a function of δ^2H_p observed at Lijiang ($\delta^2H_{P\_OBS}$). Next 3 columns: Correlation coefficients and slopes of the 3 different contributions based on the δ^2H_v simulated by SWING2 models as a function of δ^2H_p simulated by SWING2 models at Lijiang at the seasonal scale.

Models		$\delta^2H_{p\_}^{OBS}$ vs $\delta^2H_{p\_SWING2}$	$\alpha' \cdot R_{veq}$	$\overline{\alpha} \cdot R_v$	$\overline{\alpha} \cdot (R_{veq}-R_v)$
GISSE_free	Slope	0.53	-	0.75	0.15
	r	0.72*	-0.57	0.99**	0.65*
GISSE_nudged	Slope	0.86	-	0.82	-
	r	0.78*	-0.29	0.88**	0.29
LMDZ4_free	Slope	0.49	-0.02	0.80	-
	r	0.65	-0.81**	0.96**	0.29
LMDZ4_nudged	Slope	0.62	-0.02	0.91	-
	r	0.87**	-0.63*	0.93**	-0.16
MIROC_free	Slope	0.58	-0.01	0.81	-
	r	0.70	-0.64*	0.96**	0.27
isoGSM_free	Slope	0.92	-	0.79	-
	r	0.91**	-0.40	0.93**	0.41
isoGSM_nudged	Slope	0.82	-	0.80	-
	r	0.85**	-0.51	0.90**	0.28
CAM2_free	Slope	0.42	-	0.91	-
	r	0.75*	-0.55	0.94**	-0.11
HadAM3_free	Slope	0.22	-0.03	0.28	0.55
	r	0.49	-0.78**	0.60*	0.84**

Notes: *, ** indicates that the correlations are significant within a 0.05 or 0.01 confidence limit. The number of samples is 12 months. Only the averaged δ^2H_p/ δ^2H_v simulated HadAM3_free and CAM_free models are from 1999 to 2001, 2001-2003, respectively. The averaged δ^2H_p simulated by other models are from 2002 to 2004.

Table 5 Correlation coefficients and slopes of δ^2H observed at Lijiang ($\delta^2H_{p\_OBS}$) and simulated by LMDZ ($\delta^2H_{p\_LMDZ}$) in precipitation and δ^2H in water vapor retrieved by IASI and simulated by LMDZ at different time scales.

Time scale		Raw data	Seasonal time scale	Intra-seasonal time scale	Synoptic time scale
$\delta^2H_{p\_OBS}$ vs	Slope	0.41	0.80	0.56	0.12
$\delta^2H_{p\_LMDZ}$	r	0.52**	0.99**	0.67**	0.15
$\delta^2H_{v\_IASI}$ vs	Slope	0.34	0.60	0.79	0.03
$\delta^2H_{v\_LMDZ\_convol}$	r	0.43**	0.74**	0.56**	0.045

Note : ** indicates that the correlations are significant within a 0.01 confidence limit. $\delta^2H_{v\_LMDZ\_convol}$ is convolved δ^2H by averaging kernels with IASI in the LMDZ model. The second term is the function of the first term in the first colum, and the correlations are based on 365 days except for the first line (76 days).

Table 6 Correlation coefficients and slopes of the 3 different contributions based on the δ^2H_v simulated by LMDZ as a function of δ^2H_p simulated by LMDZ at Lijiang at different time scales

Time scale		$\alpha' \cdot R_{veq}$	$\bar{\alpha} \cdot R_{vLS}$	$\bar{\alpha} \cdot (R_{veq} - R_{vLS})$	RH vs $\bar{\alpha} \cdot (R_{veq} - R_v)$
Raw data	Slope	-	0.67	0.31	0.50
	r	-0.21	0.82**	0.57**	0.24
Seasonal time scale	Slope	-	0.79	0.16	-0.88
	r	-0.89**	0.99**	0.78**	-0.59**
Intra-seasonal time scale	Slope	-	0.39	0.62	0.92
	r	-0.003	0.69**	0.87**	0.35**
Synoptic time scale	Slope	-	0.69	0.32	0.58
	r	0.09	0.77**	0.50**	0.30

Notes: *, ** indicates that the correlations are significant within a 0.05 or 0.01 confidence limit. $\delta^2H_{v\_lmdz\_convol}$ is convolved δ^2H by averaging kernels with IASI in the LMDZ model. RH represents the relative humidity at Lijiang

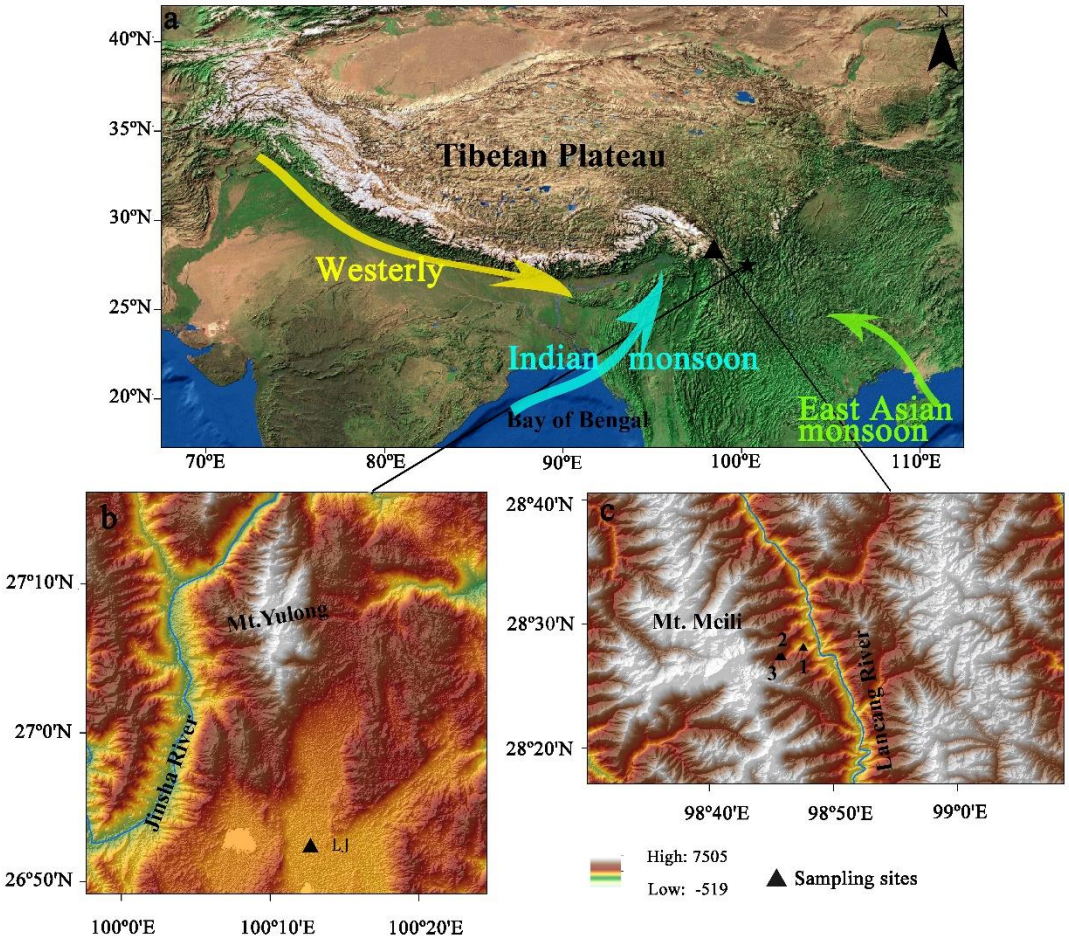

Figure 1. a) Map showing the location of the sampling stations at the scale of the TP. The pentagram stands for Mount Yulong (Mt. Yulong) and the triangle stands for Mount Meili (Mt. Meili). Arrows show the two main air mass trajectories bringing water vapor to the South-Eastern TP: monsoon winds from the Bay of Bengal (blue arrow) and from the South China Sea (green arrow), and Westerly winds (yellow arrows). b) The location of Lijiang station (LJ). c) The location of Meili stations (The numbers with black solid triangle refer to stations where the isotopic data of precipitation are obtained. 1, MY; 2, TZ; 3, LH).

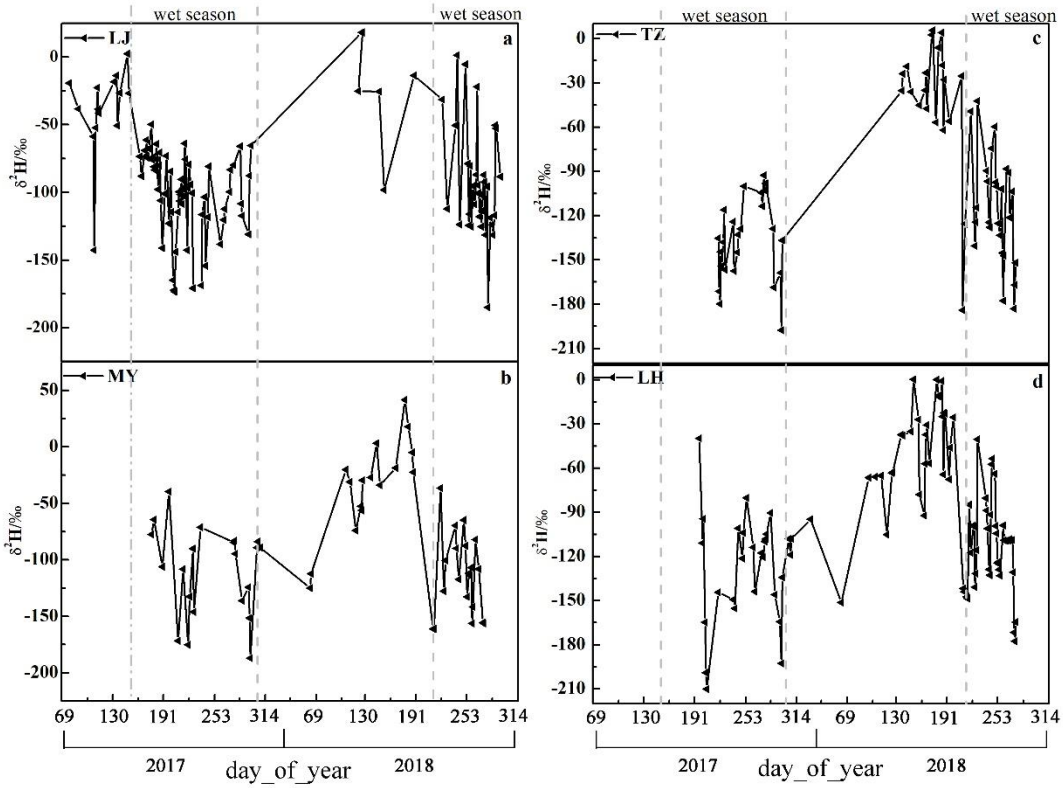

Figure 2. Daily changes in precipitation δ^2H in Mount Yulong region at Lijang (LJ) (a) and Mount Meili region at Mingyong (MY) (b), Taizimiao (TZ) (c), Lianhuasi (LH) (d) from the 2017-2018 period.

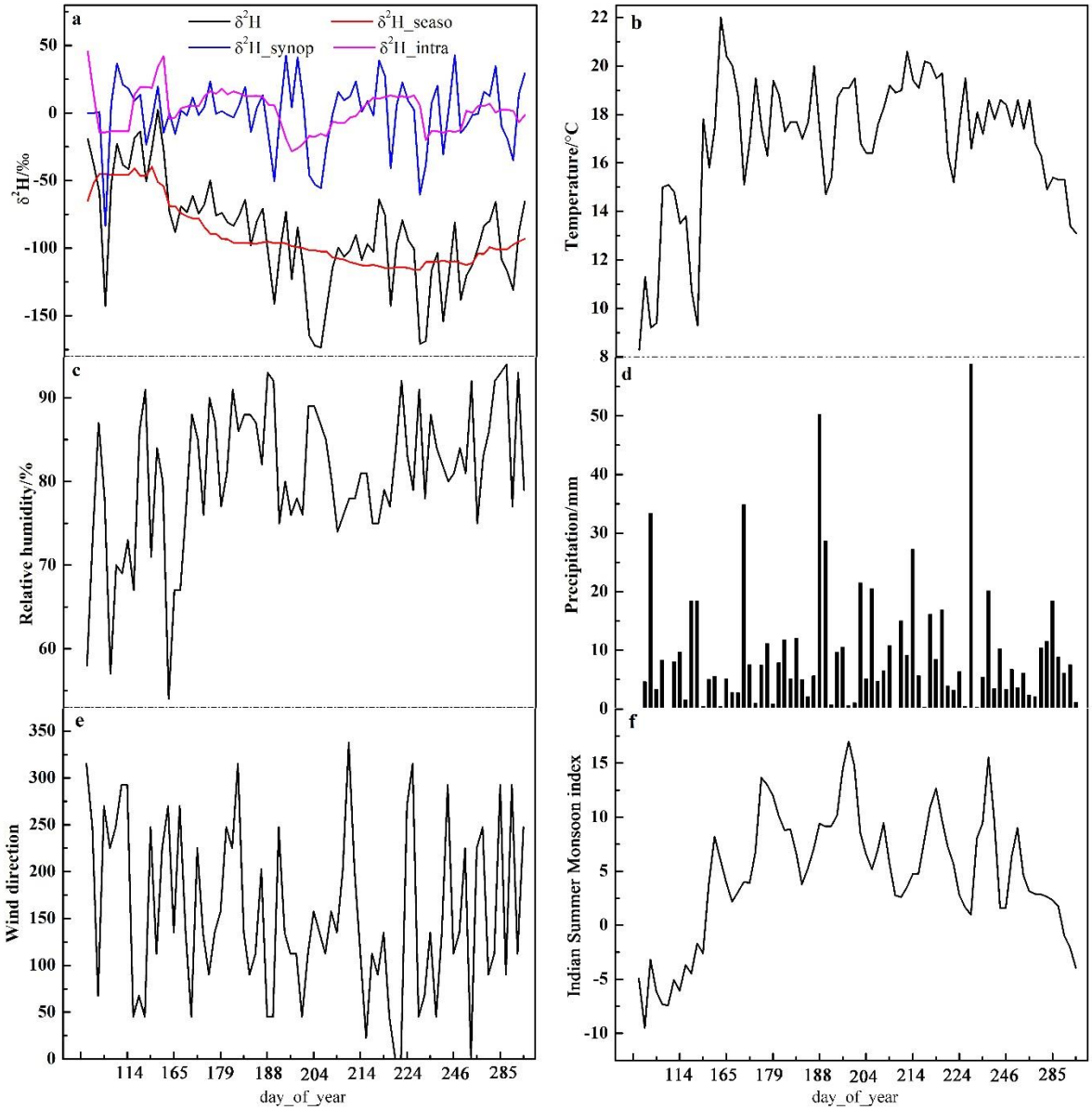

Figure 3. Time series of raw daily δ^2H in precipitation at Lijiang (a, black) and the filtered time series at the seasonal (a, red), intra-seasonal (a, magenta) and synoptic (a, blue), temperature (b), relative humidity (c), precipitation amount (d), wind direction (e) and Indian Summer Monsoon Index(f). All time series are for the year 2017 only.

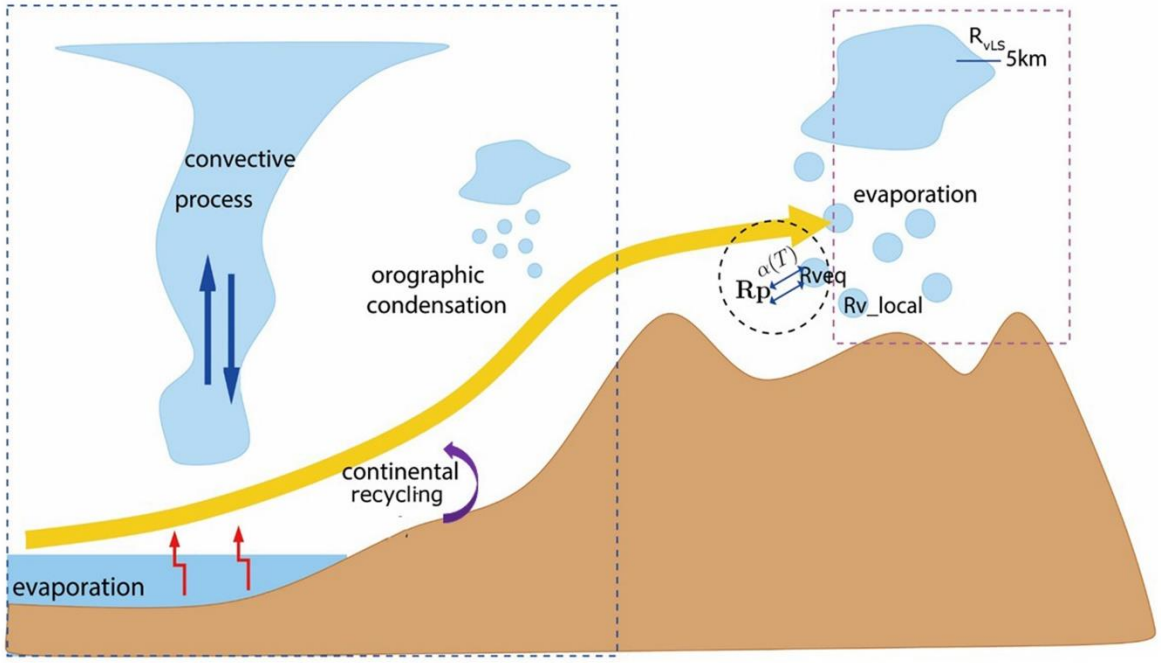

Figure 4. A schematic to illustrate how the δ^2H in precipitation is decomposed into three different contributions. Each colored box represents an ensemble of physical processes. The blue dashed box represents the variations in water vapor δ^2H, which reflects the effects of many processes along air mass trajectories including deep convection; the black dashed circle represents the effect of variations in the precipitation - vapor equilibrium fractionation factor; the magenta dashed box represents a combination of precipitation-vapor disequilibrium effects, including fractionation during rain evaporation, variations in the vertical gradients between the surface and 5 km (where the water vapor δ^2H is observed by IASI) and small-scale variations in water vapor δ^2H (leading to differences between the water vapor δ^2H observed by IASI and that with which the precipitation locally equilibrates).

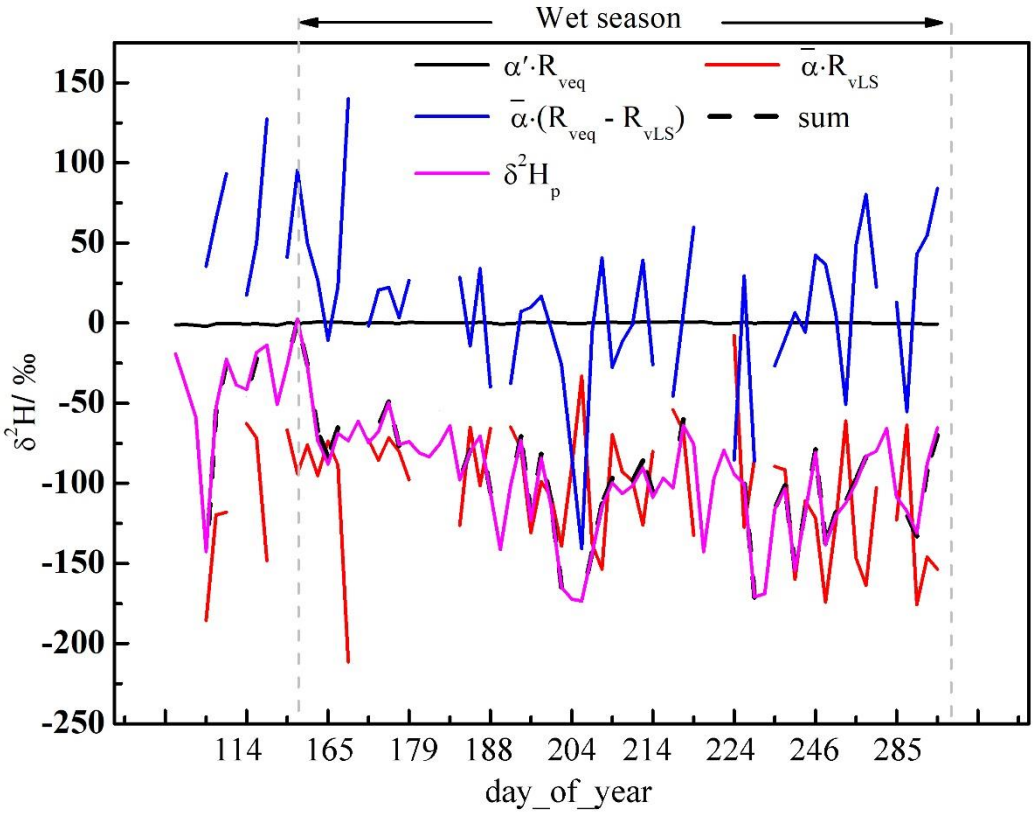

Figure 5. Raw time series of δ^2H_p (magenta) and its different contributions : $\alpha' \cdot R_{veq}$ (solid black), which represents the effect of temperature variations on precipitation-vapor equilibrium fractionation coefficient, $\overline{\alpha} \cdot R_{vLS}$ (red), which represents the ensemble of processes along air mass trajectories that affect the water vapor at the large scale (δ^2H_{vLS}), and $\overline{\alpha} \cdot \left(R_{veq} - R_{vLS}\right)$ (blue), which represents the ensemble of processes that transform the δ^2H_{vLS} variability into the δ^2H_p variability (see text and Fig. 4). The sum of the 3 contributions (dashed line) yields the initial raw precipitation time series, confirming that our decomposition is correct.

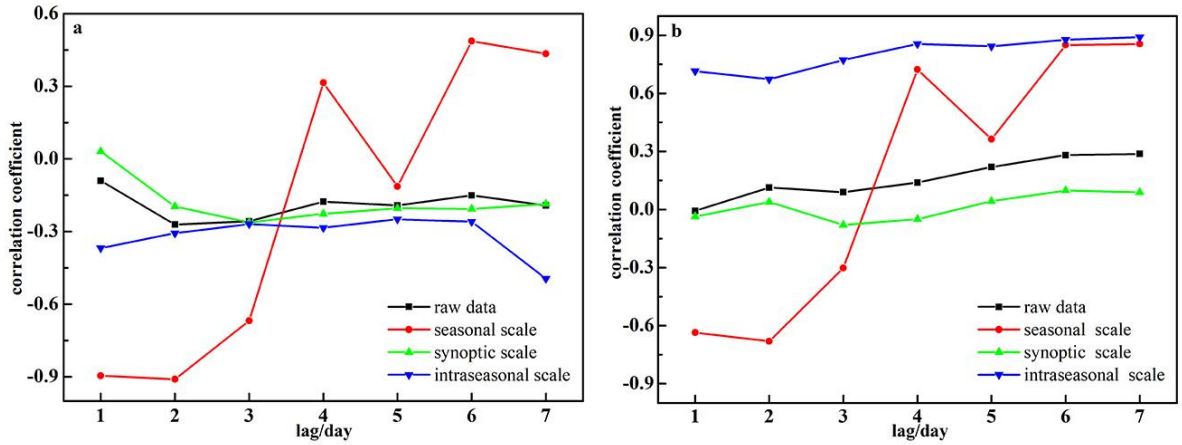

Figure 6. Correlation coefficients between δ^2H and cumulated precipitation along the mass air trajectory as a function of lag at the different time scales for observed δ^2H in precipitation at Lijiang (a) and for δ^2H in vapor retrieved by IASI (b). For example, for a lag of 3, the correlation coefficient is calculated between δ^2H_p and the precipitation cumulated during the 3 previous days along the trajectory.

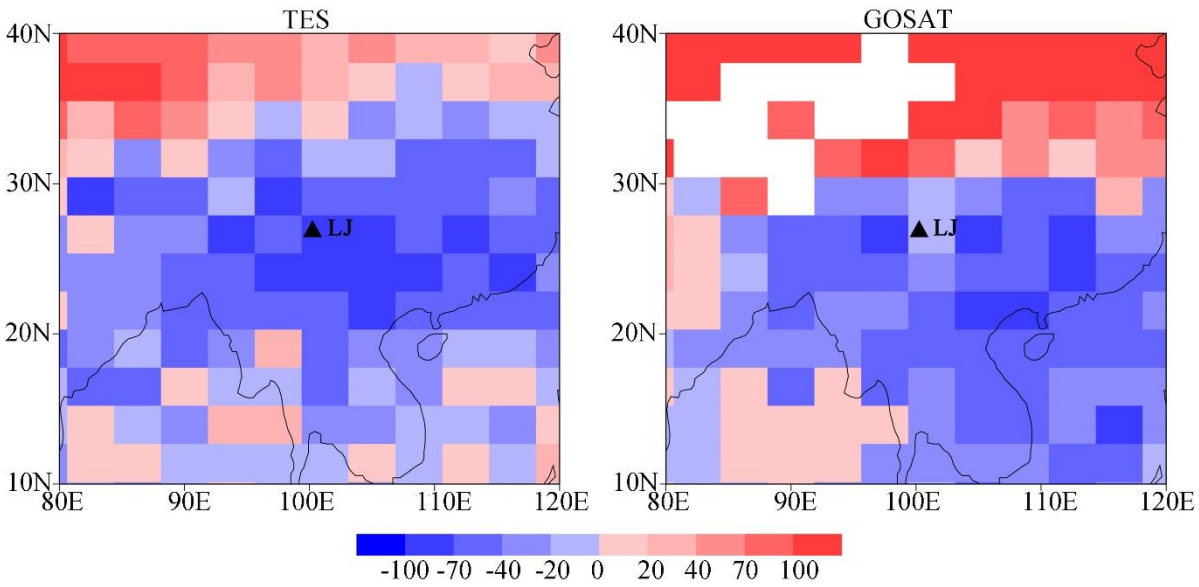

Figure 7. Map of JA-MA (July-August minus March-April) difference in water vapor δ^2H retrieved by TES and GOSAT.

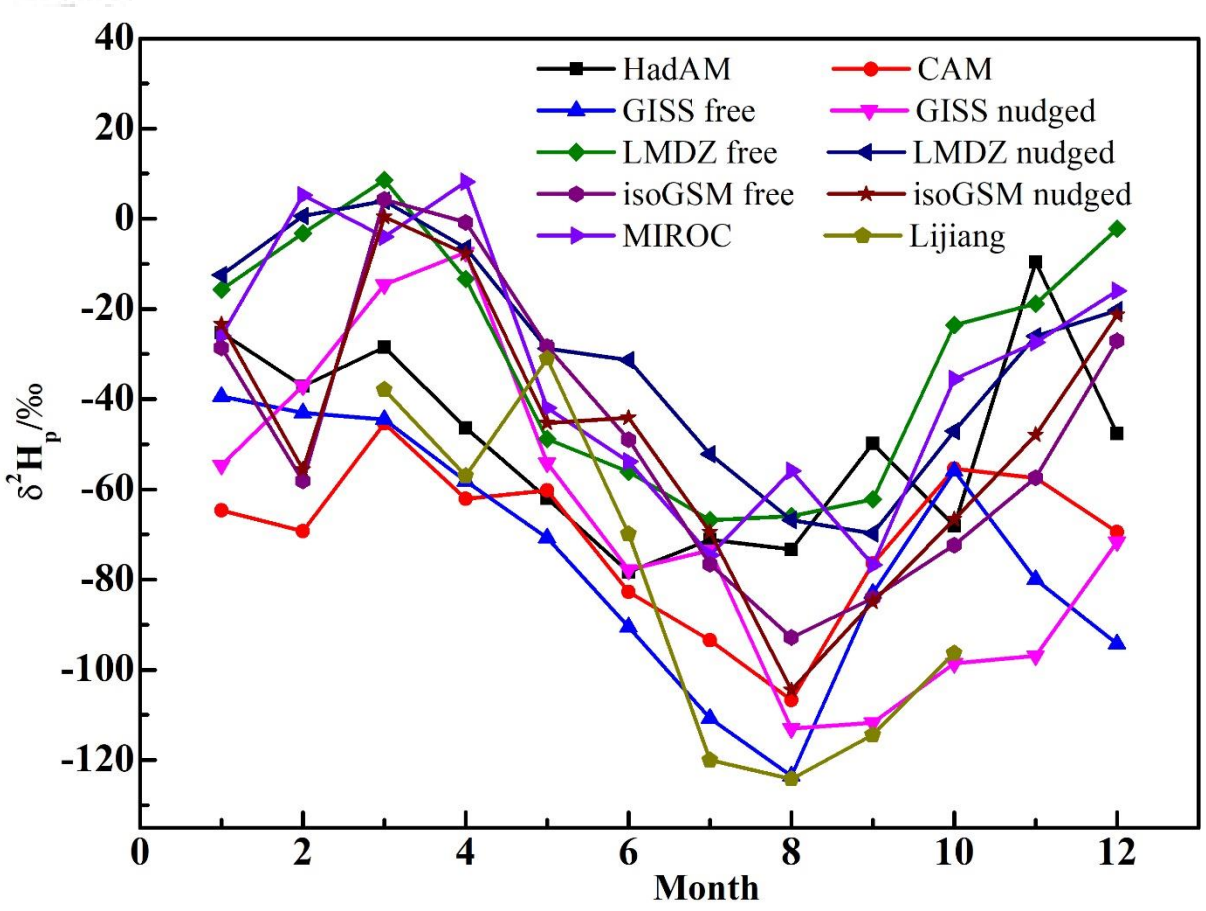

Figure 8. Seasonal cycle of δ^2H in precipitation simulated by the SWING2 models.

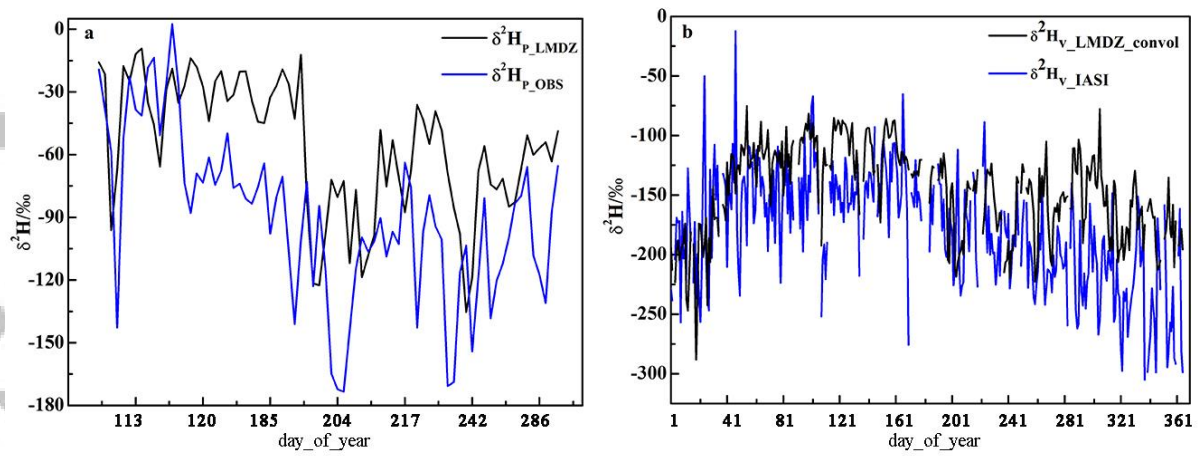

Figure 9. Daily time series of δ^2H in precipitation observed at Lijiang and simulated by LMDZ (a) and δ^2H in the water vapor retrieved by IASI and simulated by LMDZ (b). $\delta^2H_{p\_LMDZ}$ and $\delta^2H_{p\_OBS}$ represent the precipitation δ^2H simulated by LMDZ and observed at Lijiang, respectively; $\delta^2H_{v\_convol\_LMDZ}$ and $\delta^2H_{v\_IASI}$ represent the δ^2H in vapor simulated by LMDZ accounting for the effect of instrument sensitivity and retrieved by IASI at 5 Km, respectively.